

THESIS

FLOW-GENERATED DISPLACEMENT OF REINFORCED GRANULAR SLOPES USING  
THE DISCRETE ELEMENT METHOD

Submitted by

Mozhdeh Dalaeli

Department of Civil and Environmental Engineering

In partial fulfillment of the requirements

For the Degree of Master of Science

Colorado State University

Fort Collins, Colorado

Fall 2017

Master's Committee:

Advisor: Paul Heyliger

Christopher Bareither

Christian Puttlitz

Copyright by Mozhdeh Dalaeli 2017

All Right Reserved

## ABSTRACT

### FLOW-GENERATED DISPLACEMENT OF REINFORCED GRANULAR SLOPES USING THE DISCRETE ELEMENT METHOD

The Discrete Element Method (DEM) has been used by researchers to study the behavior of granular material. It is based on the discrete nature of the granular media and tracks the displacements of individual particles and their interactions at every time-step of the simulation.

This approach was used in this study to investigate the flow-generated displacement of spring-reinforced planar granular slopes. A Discrete Element (DE) code was created using MATLAB and FORTRAN to carry out the simulations. The code was validated by comparison of simulation results with analytical solutions.

Granular slopes with particle radii ranging from 5 to 10 *mm* and various initial slopes were generated. Reinforced slopes were created by adding reinforcement, in the form of linear springs restraining surface particles, to the original geometry. The surface of both the original and the reinforced slopes was exposed to flow-generated drag forces. Various reinforcement patterns were modeled and the resulting flow-generated displacements were measured and studied. It was found that slope reinforcing can either delay or prevent flow-generated movements and the effectiveness of the reinforcing depends on the slope of the packing, the magnitude of the drag force and the pattern of the reinforcing.

## ACKNOWLEDGEMENTS

I would like to thank my advisor, Dr. Heyliger, for giving me this opportunity and for his continuous support throughout the research and the thesis completion process.

I would also like to thank Kirsten Peterson for her help and involvement.

This research utilized the CSU ITeC Cray HPC System supported by NSF Grant CNS-0923386.

## DEDICATION

To my parents, for their endless love and support.

To Ali and his parents.

## TABLE OF CONTENTS

ABSTRACT.....	ii
ACKNOWLEDGEMENTS.....	iii
DEDICATION.....	iv
LIST OF FIGURES.....	vi
NOTATION AND DEFINITIONS.....	viii
1. INTRODUCTION.....	1
1.1 Objectives.....	6
2. LITERATURE REVIEW.....	7
2.1 DEM Algorithm Properties.....	7
2.1.1 Contact Force Models.....	7
2.1.2 Contact Detection Algorithm.....	9
2.1.3 Specimen Generation.....	10
2.1.4 Particle and Boundary Properties.....	12
2.2 Validation of DE Simulations.....	14
2.3 DEM Applications.....	15
3. THEORY OF THE DISCRETE ELEMENT METHOD.....	19
3.1 Assumptions.....	19
3.2 DEM Algorithm and The Calculation Cycle.....	20
3.3 Time Increment.....	21
3.4 Spherical Particles.....	22
3.5 Contact Models.....	22
3.6 Energy Dissipation and Global Damping.....	27
3.7 Application of Newton's Law of Motion.....	28
4. METHODS.....	31
4.1 Specimen Generation.....	31
4.2 Munjiza NBS Contact Detection.....	36
4.3 Surface Reinforcement.....	37
4.4 Flow-Generated Forces.....	39
4.5 Model Properties.....	40
5. RESULTS AND DISCUSSION.....	41
5.1 DEM Validation.....	41
5.1.1 Collision of a Particle with a Rigid Wall.....	41
5.1.2 Collision of Two Particles.....	47
5.2 PARAMETRIC STUDY.....	51
5.2.1 Packings with Various Particle Size Distributions.....	51
5.2.2 Packings with Identical Particles.....	59
6. Summary and Conclusions.....	68
REFERENCES.....	71
APPENDIX A.....	74

## LIST OF FIGURES

Figure 3-1 DEM algorithm .....	21
Figure 3-2 Contact force model .....	23
Figure 3-3 Contribution of particle velocities to relative normal and tangential velocities .....	25
Figure 4-1 Specimen generation steps, (a) triangular mesh based on Delaunay triangulation of random points, (b) incircles of the triangles, (c) vertex infilling, (d) secondary incircles.....	32
Figure 4-2 Settling of particles under gravity .....	33
Figure 4-3 Particle packings with varying initial slopes, created using the triangulation method	34
Figure 4-4 Packings with an identical particle group and varying slope .....	35
Figure 4-5 Particle size distribution of 350 particle packings .....	35
Figure 4-6 Example of particle mapping using the NBS method, (a) for each row of cells, the ascending list of the particle numbers is created (b) the lists are stored in arrays A and B as linked lists .....	37
Figure 5-1 Force models for a particle-wall collision.....	42
Figure 5-2 $\Delta(t)$ and $y(t)$ .....	42
Figure 5-3 Effect of contact damping on the particle-wall collision .....	44
Figure 5-4 Effect of time-step on simulation error for $\alpha=0$ and $\beta=0.01$ .....	45
Figure 5-5 Effect of time-step on simulation error for $\alpha=0$ and $\beta=0.1$ .....	45
Figure 5-6 Effect of global damping on the particle-wall collision without contact damping .....	46
Figure 5-7 Effect of global damping on the particle-wall collision with contact damping .....	47
Figure 5-8 Force models for a particle-particle collision.....	47
Figure 5-9 Simulation error in calculation of $x_1$ , for various contact damping coefficients.....	49
Figure 5-10 Particle velocities during collision for various contact damping coefficients .....	50
Figure 5-11 Percent change in momentum of the system.....	51
Figure 5-12 Percent change in kinetic energy of the system .....	51
Figure 5-13 Average flow-generated displacement of surface particles of unreinforced packings .....	52
Figure 5-14 Average flow-generated displacement of surface particles at $t=3\text{sec}$ .....	53
Figure 5-15 Average flow-generated displacement of surface particles of unreinforced packings with the same particle size distribution.....	53
Figure 5-16 Particle packings reinforced with the net pattern.....	55
Figure 5-17 Particle packings reinforced with the 25% shallow reinforcing pattern .....	56
Figure 5-18 Particle packings reinforced with the 25% deep reinforcing pattern .....	57
Figure 5-19 Particle packings reinforced with the 50% deep reinforcing pattern .....	58
Figure 5-20 Time-averaged flow-generated displacements of the surface particles for packings	59
Figure 5-21 Percent Change in Average Flow-Generated Displacement of Surface Particles.....	59
Figure 5-22 Reinforced packings with the same particle size distribution.....	60
Figure 5-23 Time-averaged flow-generated displacements of surface particles of unreinforced and reinforced packings with the same particle size distribution .....	61
Figure 5-24 Percent change in average flow-generated displacement of surface particles for packings with the same particle size distribution .....	62
Figure 5-25 Percent change in average flow-generated displacement of surface particles for packings with the same particle size distribution due to %10 increase in drag force.....	63

Figure 5-26 Average flow-generated displacement of surface particles of unreinforced 12.9° slope .....	63
Figure 5-27 Time-averaged flow-generated displacements of unreinforced and reinforced packings with the same particle size distribution for H=3.2 N/m .....	64
Figure 5-28 Percent change in flow-generated displacements of packings with the same particle size distribution for H=3.2 N/m .....	65
Figure 5-29 Maximum tension force in reinforcing springs for packings for H=4.0 N/m .....	65
Figure 5-30 Time-averaged flow-generated displacements of unreinforced and reinforced packings with the same particle size distribution for H=4.0 N/m .....	66
Figure 5-31 Percent change in flow-generated displacements of packings with the same particle size distribution for H=4.0 N/m .....	66
Figure 5-32 Percent change in flow-generated displacements of unreinforced and reinforced packings with the same particle size distribution due to 25% increase in the drag force .....	67
Figure A-1 Particle size distribution of packings shown in Figure 4-3 .....	74

## NOTATION AND DEFINITIONS

$K_n$	= Normal contact spring stiffness
$K_t$	= Tangential contact spring stiffness
$\hat{n}$	= Unit vector in the normal direction
$n_x$	= $x$ component of unit vector $\hat{n}$
$n_y$	= $y$ component of unit vector $\hat{n}$
$\hat{t}$	= Unit vector in the tangential direction
$c$	= Cohesion
$d$	= Distance between the centers of two disks
$\Delta T$	= Time increment
$\Sigma \vec{F}(i)$	= Resultant force applied to particle $i$
$\vec{F}(i, j)$	= Contact force vector applied to particle $i$ due to contact with particle $j$
$\vec{F}_B(i)$	= Body force applied to particle $i$
$\Sigma \vec{F}_E(i)$	= Sum of the external forces applied to particle $i$
$\vec{F}_D(i)$	= Global damping force applied to particle $i$
$I(i)$	= Mass moment of inertia of particle $i$
$m(i)$	= Mass of particle $i$
$\tau(i, j)$	= Torque applied to particle $i$ due to contact with particle $j$ , positive counterclockwise
$\tau_D(i)$	= Global damping torque applied to particle $i$
$n$	= Total number of particles
$\vec{P}(i)$	= Position of particle $i$
$r(i)$	= Radius of disk $i$
$\Delta V_n$	= Normal component of the relative velocity of contact
$\Delta V_t$	= Tangential component of the relative velocity of contact
$T$	= Time
$\vec{V}(i)$	= Velocity of particle $i$
$\alpha$	= Global damping coefficient
$\beta$	= Particle-particle and particle-wall contact damping constant
$\theta(i)$	= Angular orientation of disk $i$
$\rho$	= Particle density
$\varphi$	= Friction angle
$\omega(i)$	= Rotational velocity of particle $i$ , positive counterclockwise

# 1. INTRODUCTION

Granular systems are composed of large numbers of particles that interact with one another and can displace independently. This results in a complex behavior that is influenced by multiple factors including but not limited to the number of particles, their physical properties, the particle size distribution of the system, and how the particles interact.

Understanding the complicated behavior of granular media is of interest in industrial, engineering, and natural applications. A better understanding of the mechanics of granular material, such as sand, gravel, aggregates, rock-fills and fractured rock, is useful in improved selection and preparation of construction sites, better management of undeveloped land, settlement and stability of structures, and mining operations (Sitharam, Dinesh and Shimizu 2002). Modern numerical tools such as DEM are able to simulate large mass movements and can be utilized to evaluate the risks of geotechnical failures such as a landslide (Soga et al. 2016). The analysis of discrete particulate systems also helps in the design of protective measures against hazards associated with slope movements such as debris avalanches (Salciarini, Tamagnini and Conversini 2010). Furthermore, improvements in the design of machinery and equipment used in the handling and storage of agricultural products, such as grains and fruits, can be achieved through a better understanding of the dynamic behavior of particulate systems (Abbaspour-Fard 2000). Other applications include design of different types of granular mixing vessels, cold compaction of metal powders, and processing of mine tailings.

Behavior of particulate systems can be studied with experimental investigations, analytical models and numerical techniques. Although demanding the most time and cost, experimental investigations provide the most valuable information about the macro-behavior of particulate

systems. Analytical techniques are based on the assumptions of material continuity and material homogeneity and therefore have limited applications. Alternatively, computer simulations are flexible and can be used in modeling a variety of granular behaviors and are the method of choice in the present work.

Experimental investigations provide valuable information and are used to calibrate or validate analytical and numerical models. However, experiments are frequently expensive, time-consuming and sometimes dangerous. Furthermore, internal stresses and displacements of individual particles cannot be measured in tests on real granular material such as sand and must usually be estimated. Contact forces and displacements of particles can only be determined if particles are made of photo-elastic material, but this type of analysis is especially time-consuming (Cundall and Strack 1979). Extrapolation of results from laboratory experiments to full scale can also be challenging.

Analytical techniques, based on the assumption that the aggregate particle geometry acts as a continuum, combined with numerical solution techniques such as the finite element method, the finite difference method and the boundary element method, have been successfully used to model soils, rocks, and other granular media. Constitutive relationships based on continuum mechanics principles are frequently used to model granular behavior. Although geotechnical analysis methods can predict geotechnical failure criteria, they are not as helpful in understanding the post-failure behavior (Soga et al. 2016). In addition, there are some aspects like non-homogeneity issues and behavior under low confining stresses that are difficult to model using continuum mechanics principles. This limits the insight offered by this method into behavior of granular material (Sitharam, Dinesh and Shimizu 2002).

The alternative approach is to model granular material as an assemblage of particles and examine granular behavior at the particle scale level. DEM, also sometimes referred to under certain conditions as the Molecular Dynamics (MD) model and originally developed by Cundall and Strack (1979), has been used for decades in the research of particulate behavior. DEM is based on the discrete nature of the granular media and tracks the micro displacements of the individual particles to get the macro behavior of the entire packing. It simplifies the problem to the equilibrium of individual particles that interact with one another at contact points.

Unlike conventional continuum approaches, numerical methods such as DEM can model and track individual particle dynamics and particle interactions at any stage of the simulation. Computer simulations demand less cost, are flexible, and can incorporate variability in size, properties, and distribution of the particles. Although numerical simulations can be time consuming to set up and are limited by computational resources, advances in computer processing speed and parallel processing techniques have made numerical models powerful tools in the analysis of particulate systems.

There are two common types of DE models dedicated to either hard particle or soft particle approach. In the hard particle model, particles are assumed to be perfectly rigid and a sequence of instantaneous collisions is processed (Zhu et al. 2007). In the soft particle approach, particles can experience multiple contacts simultaneously, and undergo minute deformations at the points of contact.

The hard particle model assumes that rigid particles follow an undisturbed motion until an instantaneous collision occurs (Luding 2008). An Event-Driven (ED) simulation method is used which discretizes the sequence of collisions. To relate the velocities after the collision to the velocities just before the collision, a collision matrix is often used which is derived from

momentum conservation and energy loss rules. Since the hard particle model ignores the details of the contact and assumes that the collisions happen one at time, it is valid when binary collision dominates and multi-particle contacts are rare (Luding 2008). The hard particle method is therefore typically used in modeling rapid granular flows (Zhu et al. 2007).

In the soft particle approach, typically used in modelling quasi-static systems, collisions or contacts happen during a series of time-steps and particles can experience multiple contacts simultaneously. It is assumed that as contact occurs, particles deform at the points of contact and develop contact forces. The deformations are used to calculate contact forces, using a force-displacement law. The velocities of the particles are assumed to be constant over a time-step, and the particles are allowed to displace. The contact forces of particles are then updated based on the changes in the displacements. The resultant force acting on each particle is then calculated and used to calculate the new particle velocities. This calculation cycle of force-displacement law and Newton's second law of motion is repeated in every time-step for every particle.

DE models can be modified to better represent a specific particulate system by selection of the appropriate particle shape and size distribution. The selected shape of the particles should be as close as possible to the actual shape of the particles under consideration since contact forces that govern the velocities and the positions of the particles are directly affected by the particle shapes. On the other hand, as the particle shape gets more complicated, the algorithms required for contact detection and contact force calculation will get much more sophisticated. This results in significant computational overhead.

The simplest DE models are planar assemblies of circular particles, also called disks. Contact detection and contact force calculations are very simple for such particles, since there is always one type of inter-particle contact. These models cannot represent the interlocking action

between the particles and frequently overestimate particle rotation since the normal forces do not affect the moment acting on the particle and frictional forces are the only forces resisting rotation.

Since almost all particulate systems in reality are three dimensional, planar models have been extended to three dimensions to account for the effect of the particle interaction in the third dimension. Three-dimensional simulations require a larger number of particles to be modeled, which calls for greater computing capacities.

Non-circular particles have been modeled in both planar and three-dimensional simulations. Typical complex shapes used to represent particles are polygons (Mirghasemi, Rothenburg and Matyas 1997), ellipses (Ng 1994), and clusters of several circular particles that have been bonded together (Abbaspour-Fard 2000). Utilization of mathematical functions to describe particle outlines, such as super-quadric particles (Cleary and Hoyer 2000), is also typical.

Using realistic particle sizes and a reasonable ratio of sample size to particle size is important in obtaining a realistic simulation. This is particularly important in modeling soil particles. When realistic soil grading is used, many small particles must be simulated for every large particle. Modeling these smaller particles significantly increases the degrees of freedom and also requires a smaller time-step to ensure stability of the system. However, the number of particles modeled in DE simulations are limited by the computational capacities. Around 10,000 particles are typically modeled in 3D simulations (Huang et al. 2014). Therefore, the use of real particle sizes in models for some of the granular media, such as soils, is generally not feasible due to computational limitations. Almost all discrete element models of soils reported in the literature have used particles that are larger than their actual sizes (Shmulevich 2010). Consequently, the particle properties should be modified to account for the difference in the particle size.

## 1.1 Objectives

The purpose of this study was to investigate the flow generated displacements of a planar assembly of disks using the DEM. One specific application of this work is to be able to model the mechanics of soils following the changes that can occur after a surface-level fire. This changes the level of plant-fiber and soil particle interaction and can dramatically influence the run-off mechanics in storms following these fires. Specific objectives were to:

- Review the existing literature on DE modeling of particulate systems
- Develop an accurate and feasible DE program to run the simulations
- Validate the DE model by comparing the results to analytical solutions
- Simulate run-off conditions for packings with various initial slopes and reinforcing patterns
- Study the flow-generated displacements and the effectiveness of the slopes reinforcement

## 2. LITERATURE REVIEW

The DEM was originally developed by Cundall and Strack (1979) as a numerical method for describing the mechanical behavior of assemblies of disks and spheres. A linear spring-dashpot model together with Coulomb friction law was used to model the particle interactions at contact points. Energy dissipation was modeled using global damping, friction and viscous contact damping so that the system could reach a state of equilibrium. The model was validated by comparison of output force plots with the corresponding plots obtained from a photo-elastic analysis applied to an assembly of disks.

The variety of the literature published on DE modeling can be generally classified into studies on DEM algorithm properties, validation of DE simulations and DEM applications.

### 2.1 DEM Algorithm Properties

A wide range of studies published on DEM are regarding DEM algorithm attributes, such as the contact force model, the contact detection algorithm, the specimen generation method, and the particle and boundary properties. These are briefly reviewed below.

#### 2.1.1 Contact Force Models

Schafer, Dippel and Wolf (1996) discussed the properties of the force laws most commonly used in DEM and compared their results with experiments on the impact of spheres. Linear-spring dashpot, Hertz, Hertz-Kuwabara-Kono and Walton-Braun models for the normal contact force were studied. For the tangential contact force, Coulomb friction, viscous friction, linear tangential spring, Walton-Braun variable tangential spring and Brilliantov slip-stick models were reviewed. Generic problems of DEM and the criteria for the right choice of the force law parameters were also discussed.

Luding (1998) discussed instantaneous and not-instantaneous collision models. In the instantaneous model, also known as the hard particle model, the velocities of the particles just before and just after the collision are of interest. This is in contrast to the not-instantaneous collision models, also known as the soft particle and DE models, which follow the trajectories of the particles during collisions by solving Newton's equation of motion and the use contact force laws. Luding explained in detail the linear spring dashpot model, the general non-linear spring dashpot model and hysteretic spring model used for modeling the normal contact forces. The viscous friction model, Coulomb friction and elastic spring models for the tangential force were also discussed.

It was shown by Luding (1998) that cluster particles more accurately model the geometry-dependent behaviors, such as particle interlock and rolling. As a result, use of cluster particles significantly reduced the excessive particle rotations and increased the shear strength of the system. Overall behavior of the system was found to be qualitatively similar to experiments involving round and angular sands.

Di Renzo and Di Maio (2004) investigated the influence of the different contact-force models on the accuracy of DEM simulations of collisions in granular flow. Elastic collision of a sphere with a flat wall was simulated using three contact-force models. A linear force-displacement model, a non-linear model for the normal direction together with a no-slip model for the tangential direction, and a non-linear model with hysteresis were used. Results were compared with experimental data in macroscopic scale, and to analytical solutions in the microscopic scale. It was shown that no significant improvement is attained using complex force models regarding the velocities after the collision. The linear model, with precisely evaluated parameters, was often equivalent with the non-linear hysteresis model and gave better results than the no-slip model. In

addition, the time evolution of the tangential forces, velocities and displacements predicted by the linear model were closer to the theoretical solution.

Krugger-Emden et al. (2007) focused on the normal contact models and reviewed a wide range of commonly used normal force schemes based on macroscopic and microscopic parameters such as the coefficient of restitution, collision time, force, displacement and velocity. The study then compared the results obtained from extended linear and non-linear force models with the experimental data on collisions of different metal alloys, ice and marble spheres reported in the literature and evaluated the accuracy and applicability of the results.

Luding (2008) described and compared the two approaches used in DE modeling of granular material based on MD methods; the soft particle and the hard particle methods. Basic force models were presented including elasto-plasticity, adhesion, viscosity, static and dynamic friction, and rolling and torsional resistance. Hard particle ED methods were also presented with an attempt to link the ED and DEM approaches in the dense limit where multi-particle contacts become important. Two- and three-dimensional simulations were discussed concerning bi-axial shearing, cylindrical shearing, and clustering in granular gases of dense assemblies, in order to illustrate the micro-macro transition towards continuum theory. The study concluded that DEM is a helpful tool in qualitative predictive modeling of the complex granular behavior.

### **2.1.2 Contact Detection Algorithm**

Cundall (1988) introduced a technique to detect contact between particles of arbitrary shape in a three-dimensional DE model. Particles considered were either convex or concave with faces that consisted of arbitrary plane polygons. Contact detection identified pairs of particles that were in contact and the geometric characteristics of the contact, such as whether faces, edges or vertices were involved and the direction of potential sliding. An efficient data structure was utilized

to allow rapid calculations for a system involving several hundred particles on a personal computer.

Munjiza (2004) explained the No-Binary Contact Search (now widely referred to as the Munjiza-NBS) method, originally developed by Munjiza in 1995. The NBS method divides the domain into cells and instead of checking every two particles for contact, only checks particles that are in neighboring cells. The cells are sized to be large enough to contain the largest particle, so that only particles from neighboring cells can have contact. The algorithm uses singly connected linked lists to map the particles into rows and columns of cells and is efficiently structured to optimize RAM and CPU requirements. The total contact detection time for the Munjiza-NBS algorithm was found to be proportional to the number of particles in the system and independent of the number of rows or columns. This is the method used for contact detection in this study and is explained in detail in Chapter Methods.

### **2.1.3 Specimen Generation**

A variety of methods have been used to generate particulate assemblies for two- and three-dimensional simulations including, but not limited to, random generation, radius expansion, gravitational approaches, triangulation and advancing front type algorithms. Each method has its own advantages and there is no agreement in the literature on which method is the optimum approach.

In the random generation approach, a random number generator is used to assign random sizes and locations to particles. Contact detection is used to reject a particle if it overlaps with the existing ones. As the domain becomes more populated, more particles will be rejected and it becomes time consuming to add new particles. A series of DEM simulations are then carried out on the system to make it denser, such as compressing the system by moving the boundaries toward

the particles. The random generation approach imposes a large computational cost for contact detection and for the iterations required to densify the system. Another disadvantage is that the particle size distribution and void ratio of the assembly cannot be controlled.

The radius expansion approach is a random non-overlapping system in which the radii of particles are expanded by a factor to achieve a certain porosity. Then a series of DEM simulations are carried out to rearrange the system and bring it into equilibrium.

Gravitational methods run DEM simulations and allow a random or a prearranged non-overlapping layout of particles to fall under a body force. Zhou et al. (2002) used a gravitational settling process on a random arrangement of spheres, followed by a discharging process, in which the spheres were dropped from the sides of the sample under gravity. In most cases, a large number of iterations are required to reach equilibrium under gravitational forces and this can result in a high computational cost. In addition, there is no control over the void ratio of the specimen created and it is difficult to create a dense sample in a pre-defined boundary such as simulating a laboratory test on a soil sample in a specific container.

Feng, Han and Owen (2003) introduced an advancing front approach to fill planar domains with disks with different radii. The advancing front algorithm was implemented in open and closed forms. The radii of the disks were randomly determined based on a size distribution function. In the closed form, the “front” is an oriented polygon obtained by joining the centers of the outermost disks. The initial front is a triangle and new disks are generated so that they are in contact with the existing disks. As the new disks are added, the front advances gradually and the specimen grows spirally outwards until it fills the domain. Since the boundaries are almost always rectangular, the major disadvantage of this method is that it leaves large gaps around the boundary. In the open

form, the initial assembly is a layer of disks along the bottom boundary, the front is open and the disks are added layer by layer until the domain is filled.

Jodrey and Troy (1985) developed an iterative algorithm for generation of random close packings of uniform spheres from a random distribution of points. An inner and an outer sphere were created at each point. The inner diameter defined the true density of the packing, which was initially very small. The outer diameter represented the nominal density and was given an arbitrary initial value. In each iteration, the inner diameter was set to the minimum center-to-center distance between any two spheres. The algorithm eliminated the largest overlap of the outer spheres by moving the particles in each step. It also slowly shrank the outer spheres until eventually the true and nominal densities matched at which point and the process was terminated.

Cui and O'Sullivan (2003) proposed a new triangulation based approach for generating a particulate specimen in two or three dimensions. The method was based on creating a triangular mesh within the boundaries and inserting the particles as the in-circles of the triangles. A mesh of tetrahedral and in-spheres were used in three-dimensions. The sensitivity of the behavior of the generated particulate system to the topology of the triangular mesh was discussed. The method was compared with the algorithm proposed by Itasca for planar systems, a modified version of the algorithm developed by Lin and Ng (1997), and the algorithm developed by Jodrey and Troy (1985) for three-dimensional systems. Relative simplicity of the algorithm and small computational cost are the advantages of the triangulation method. However, it was not as effective in creating dense three-dimensional assemblies as the other typically used approaches.

#### **2.1.4 Particle and Boundary Properties**

Jensen et al. (1999) investigated the effects of surface roughness and particle shape in DE simulations of granular media-structure interface. Several simulations of the ring shear test were

carried out with varying normal loads, roughness of the shearing surface, and particle types (clustered and non-clustered). Particles of general shape were modeled by combining several smaller circular particles into clusters that act as a single large particle. Periodic boundaries were used in the simulations to increase computing efficiency and avoid deleterious boundary effects. Periodic boundaries allow particles to pass out of the boundary on one side and reappear on the opposite boundary. It creates an infinite control volume and removes boundary effects. This is particularly helpful when the number of particles simulated are limited due to computing capacity.

Ferrellec and McDowell (2010) introduced a new method to model complex irregular particle shapes in DE models using overlapping spheres. The effects of the parameters used on the accuracy of shape reproduction and the number of particles involved were discussed. Since overlapping spheres cause a non-uniform density in the particle, a method to reduce the error in the principal moments of inertia of the particle was also discussed. Pullout tests were then simulated to analyze the interaction between ballast and geo-grid and it was found that the ballast geo-grid interlocking is better simulated using the proposed method than using simpler particle shapes.

Huang et al. (2014) studied the effect of sample size on the response of the DEM simulations when a realistic particle grading was used. Four DE simulations of tri-axial compression tests with an identical initial void ratio and stress state were used. Three differently sized samples with rigid cylindrical boundaries were compared with a sample with periodic cubic boundaries. The number of particles in the samples ranged from 6,783 to 20,164. It was shown that the rigid boundaries resulted in an inhomogeneity in the density of samples whereas the application of periodic boundaries may be beneficial as it yielded a more homogeneous sample and was more likely to represent real material response. The study concluded that when rigid

boundaries are used, the sample size should be large enough so that the boundary constraint does not affect the overall behavior of the system.

## **2.2 Validation of DE Simulations**

Ting et al. (1989) validated the planar disk-based DE approach by simulating standard geotechnical laboratory tests, including the one dimensional compression, direct simple shear, and tri-axial tests. Reduced scale models were used for simulating full scale bearing capacity and lateral earth pressure tests to overcome computational limitations. The geotechnical centrifuge modeling principles were used to ensure stress-strain-strength similitude between the model and the prototype. It was shown that although the planar DE model overestimated the effect of the individual particle rotation, it could simulate non-linear stress-history-dependent soil behavior realistically if individual particle rotation were inhibited.

Li, Xu and Thornton (2005) carried out DE simulations of sand-piles and assessed model validation by comparing the profile and the angle of repose with laboratory experiments. Simulations were carried out for quasi-two-dimensional and axisymmetric three-dimensional arrangements. The contact force model was based on Hertzian theory for normal contacts and was based on the Mindlin–Deresiewicz theory for tangential contacts<sup>1</sup>. Polydisperse glass beads were used for the experiments. Simulations and experiments were also carried out for three-dimensional conical piles of smooth monodisperse steel balls. To ensure consistency of the simulations with physical experiments, sliding friction was measured experimentally and the resulting value of the friction coefficient was used for the particle-particle and particle-wall interactions in the DEM

---

<sup>1</sup> The Hertz-Mindlin and Deresiewicz model is based on the application of the elastic theory to the contact between two elastic spheres. It consists of a non-linear elastic normal force-displacement relationship developed by Hertz together with Mindlin and Deresiewicz's modification to Hertz's theory in the tangential direction.

simulations. It was shown that the simulation results were in good agreement with the experimentally determined profiles and the measured angle of repose.

Hungr (2008) verified simplified models of spreading flow against controlled laboratory experiments using dry granular materials. Results of simulations with alternative assumptions, regarding the distribution of earth pressure in the material, were compared with the results of a series of dam-break experiments with different slope angles and bed materials. It was shown that assumptions regarding internal friction of particles, typically used in previous works, could cause substantial errors and modifications to the assumptions that were proposed.

Grima and Wypych (2011) developed and validated calibration methods for DE modeling. Results of DEM simulations for cohesion-less and cohesive granular materials were checked against experimental slump and hopper discharge tests to validate static and rolling coefficients of friction and the coefficient of restitution. Single particle properties were measured to develop an appropriate particle shape representation and size distribution. Simulations that modeled the experiments were carried out to replicate the flow mechanisms and a trial-and-error process was conducted by altering dependent parameters such as rolling friction and cohesion energy.

### **2.3 DEM Applications**

Campbell and Brennen (1983) simulated Couette flows of granular materials using a planar unidirectional flow model of inelastic disks. The collisions were assumed to be instantaneous and departing velocities were calculated based on the incident velocities and a coefficient of restitution was used to represent the inelasticity of the collisions. Interstitial fluid and gravitational effects were neglected. Results were compared with theoretical constitutive models and with experimental results.

Matuttis, Luding and Herrmann (2000) studied DEM simulations of heaps made of spherical and non-spherical particles. Quasi-static granular assemblies were modeled using smooth spherical and polygon particles. The piles were either constructed layer-wise or from a point source, in a so-called wedge sequence, which is similar to depositing granulates from a conveyor belt. The distribution of the stress under the heaps, arching phenomenon and stress chains were observed in the simulations. It was found that for spherical particles, the structure of the contact network and orientation was correlated to the stress state. Also for smooth particles, regardless of the contact-force law or the particle shape, small variations in boundary conditions or particle sizes could lead to arching or formation of a dip. For polygonal particles with friction, it was shown that the angle of repose depends on the construction history and the polydispersity of the material.

Isotropic compression and tri-axial static shear tests under drained and undrained stress paths were modeled by Sitharam, Dinesh and Shimizu (2002) using a three-dimensional DE model. Poly-disperse 1000-particle assemblies of loose and dense spheres were modeled and periodic boundaries were used to represent an infinite three-dimensional space. The evolution of the internal variables such as average co-ordination number and induced anisotropy during deformation were studied. The macroscopic behavior of the assemblies in drained and undrained shear tests were investigated. It was found that the DEM simulations were capable of realistically reproducing the behavior of the granular assemblies. Although numerical simulations highlighted the effect of the inter-particle friction on the behavior of the granular media, the results clearly indicated a non-linear correlation between the specific volume and the logarithmic mean principle stress. It was also observed that at a given density, shearing or change in the stress ratio results in loss of contact and therefore there appears to be a constant limiting value of contact anisotropy that a given system can sustain.

Zhou et al. (2002) studied the angle of repose of granular materials using a modified three-dimensional DE simulation incorporating a rolling friction model. The effect of the different variables related to the particle, material and geometric properties on the angle of repose were studied. It was shown that sliding and rolling friction were the primary factors affecting the formation of sand-piles. Particle size and container thickness were found to significantly affect the angle of repose, while density, Poisson's ratio, damping coefficient and Young's modulus were found to have less influence. The particle-particle and particle-wall interaction mechanisms that underlie these behaviors were discussed and empirical equations that relate the affecting variables to the angle of repose were suggested for engineering applications.

Liu (2006) simulated the Direct Shear Box Tests (DST), a common experiment for determining the shear strength of soils, using DEM. Loose two-dimensional samples of 3259 particles were modeled. The numerical data of the simulations were used to interpret the angle of internal friction and a planar stress-dilatancy equation for the mobilized plane in the system. The study addressed the intrinsic drawbacks involved in performing and interpreting the conventional DST, such as the influence of the frictional force between the inside surface of the upper shear box and the sample on the measured shear strength.

Shmulevich (2010) explained DEM in general and provided state of the art modeling of soil-tillage interaction using two- and three-dimensional DE simulations. The applicability of DEM for use in the optimization of soil-tillage interaction was presented by several case studies and the limitations and advantages of the method were discussed.

Use of particulate DEM in geotechnical research was reviewed by O'Sullivan (2011). The background of the method, evolution of the use of DEM in geomechanics, the general principles of the algorithm, calculation of contact forces, formulation of boundary conditions, interpretation

and post-processing of results, validation approaches, and application to field-scale problems were discussed. The article gave a comprehensive overview of the application of DEM to researchers in geomechanics interested in adopting the method in their studies.

Marketos and O'Sullivan (2013) proposed a new method for analyzing wave propagation through granular material using DEM. A two-dimensional un-damped assembly of uniformly sized circular particles was modeled and a linear spring contact scheme was used. The stiffness and mass matrices of the granular sample were created and used to calculate its modes of vibration, natural frequencies and its transfer function.

There are a host of other applications that have been the subject of DEMs, but those cited here are the most relevant to the present study. There have been very few, if any, studies of particulate media in which the particles have been reinforced with other structural elements while being subjected to hydraulic forces. Both of these features are prominent additions to existing work and form much of the novelty of the results that follow.

### 3. THEORY OF THE DISCRETE ELEMENT METHOD

DEMs simulate the behavior of granular systems by tracking movements of individual particles. It is a dynamic or transient simulation based on equilibrium of particles which evolves over discrete time increments during which the acceleration of particles is assumed to be constant.

DEM calculations are based on the application of a force-displacement law and Newton's second law of motion. A small amount of overlap is typically allowed at contact points that represents particle deformations. The magnitude of this overlap is related to a contact force using a force-displacement law and a time-dependent numerical solution of Newton's equation of motion is then carried out to calculate particle movement.

The theory of DEM is presented in this chapter. The basic assumptions, time-stepping and the calculation cycle of the DEM algorithm, and the required time increment are all discussed. After that, the scheme used in this study is explained including the use of spherical particles, the contact force model, energy dissipation, and the application of Newton's law of motion.

#### **3.1 Assumptions**

Most DE models follow the approach of Cundall and Strack (1979) and are based on the following basic assumptions for both two- or three-dimensional packings and regardless of the selected particle shapes, particle size distribution, contact force model, and boundary conditions.

DEM traces movements of individual particles of an assembly by calculating equilibrium contact forces. A disturbance, caused by a displacement of boundaries or application of external forces to particles, propagates through the granular medium from particle to particle. It is assumed that the time-step chosen is small enough and disturbances can only spread from one particle to its immediate neighbors during a single time-step.

Particles are assumed to deform at points of contact with other particles or the boundaries. Deformations are represented by overlap of the boundaries and are assumed to be small in relation to particle sizes. There are no plastic deformations that remain after the complete separation of particles, so that particle shape is conserved throughout the simulation. In other words, particles are assumed to collide through a new un-deformed contact point every time a new contact occurs.

In reality, particle-particle or particle-boundary contacts occur over a finite surface area. Most DEM approaches assume that the contact area is small compared to the surface area of the contacting bodies and that contact occurs at a point at the centroid of the contact surface. The contact forces and torques are point loads acting at the contact point.

In the numerical integration of Newton's law of motion, it is assumed that particle velocities and accelerations are constant during a time-step. It is also assumed that no new contact is assumed to develop during a time-step, and the contact forces acting on each particle only result from the contacts detected at the beginning of the current time-step.

### **3.2 DEM Algorithm and the Calculation Cycle**

An overview of the sequence of calculations in a DEM algorithm is presented in Figure 3.1. Once the initial geometry of the particulate system is defined, the simulation goes through a series of time-steps. For every time-step a cycle of calculations is completed to update the position and velocity of the particles. The cycle starts with contact detection between neighboring particles. Next, for every pair of contacting bodies the relative velocities and contact overlaps are calculated and the contact force is determined based on a force-displacement law. After this has been accomplished for all contacts, the resultant forces for each particle are calculated. Assuming that the accelerations are constant during the time-step, Newton's law of motion is applied to update

the particle position and velocity and the calculation cycle is complete. The cycle is repeated for the next time-step beginning with contact detection.

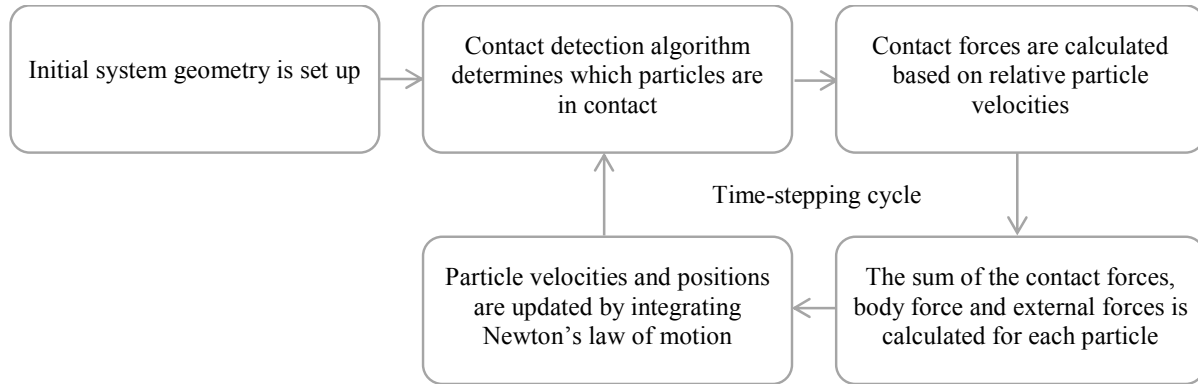


Figure 3-1 DEM algorithm

### 3.3 Time Increment

The choice of an appropriate time increment is important in the execution of a DE simulation. The time increment should be small enough to ensure stability and accuracy of the numerical simulation and justify the assumption of constant velocity and acceleration (See Section 3.2). On the other hand, a larger time increment means fewer time-steps and increases computational efficiency.

Cundall and Strack (1979) required the time increment to be taken as a fraction of the critical time-step of  $2\sqrt{m/k}$  to ensure stability of the numerical scheme, where  $m$  is the mass of the particle and  $k$  is the stiffness of the spring representing the contact force. The critical time-step proposed is  $1/\pi$  of the period of oscillation for an un-damped single degree-of-freedom spring-mass system, which is  $2\pi\sqrt{m/k}$ .

For many DE simulations the time increment is chosen so that a typical collision consists of 10 to 20 time-steps (Shmulevich 2010). Schafer, Dippel and Wolf (1996) argued that there is no intrinsic time-scale to collisions and the choice of the time increment depends on the maximum

relative velocities expected during the simulation and recommended 100 time-steps during a collision to ensure numerical accuracy. A time step of  $10^{-6}$  sec was used in the present study, equal to  $0.003\sqrt{m/k}$  for the smallest particle, to ensure stability of the system and maintain precision of calculations.

### **3.4 Spherical Particles**

Spherical particles have been used in many DE simulations with various contact force laws. The dynamic behavior of large granular assemblies can be modeled reliably using spherical particles, and qualitative and quantitative agreement with experiments have been reported.

The primary advantage of using spherical particles is the straightforward contact detection, which is simply comparing the distance between the center of the particles and the sum of their radii. The numerical efficiency due to the simple contact detection allows simulating larger granular assemblies with more particles and more detailed numerical investigations, such as variation of material properties, boundary conditions, and other parameters.

One disadvantage of this approach is that spherical particles do not interlock as most real angular particles do. Particle interlocking contributes to tangential contact forces that are specifically important in modeling of quasi-static systems. Therefore, to effectively model static phenomenon using spherical particles, tangential force parameters, such as damping constants, should be determined by comparison of simulation results with experiments (Poschel and Schwager 2005).

### **3.5 Contact Models**

One of the most important characteristics of a DEM simulation is its contact model, also called the contact constitutive model, which determines the force-displacement relationship

between contacting bodies. The contact model should be chosen to closely represent the behavior of the simulated material.

Many contact force schemes have been suggested and used in DE simulations. Contact forces are nearly always decomposed into normal and tangential components with respect to the contact surface. The contact force models used for normal contact can be generally classified into linear spring-dashpot model, non-linear viscoelastic models, and hysteretic spring models. The normal force is associated only with the translational motion of the contacting particles, whereas the tangential force is associated with the rotational motion of the particles in addition to the translation motion.

The tangential contact force is mainly determined by the surface properties of the particles and the inter-locking of the small surface asperities. It is typically modeled in DE simulations using sliding and rolling frictions. Therefore, it is also closely related to energy dissipation of the system, which is essential to the equilibrium of quasi-static simulations.

The simulations carried out for this study were based on the contact models used by Cundall and Strack (1979). A no-tension linear spring-dashpot model is used in the normal direction and a linear spring-dashpot model, combined with Coulomb friction law is used in the tangential direction. Figure 3-2 schematically shows the contact model used.

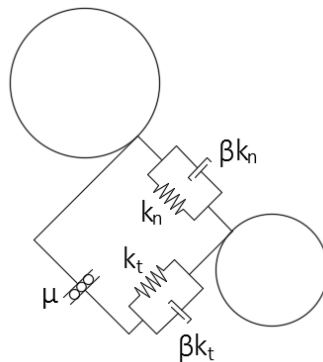


Figure 3-2 Contact force model

The following discussion explains in detail the contact force calculations for two contacting disks that are referred to as disks  $i$  and  $j$ . A similar approach is used in the case of a disk contacting a wall. A complete list of the notation used in this section and their definitions is presented on page viii. The superscripts represent the time associated with the variable and the subscripts represent vector components. For instance,  $\vec{A}_x^T$  is the  $x$  component of the vector  $\vec{A}$  at time  $T$ .

The disks are in contact if the distance between the centers of the disks,  $d$ , is smaller than the sum of the disks' radii:

$$d = |\vec{P}(j) - \vec{P}(i)|$$

$$d < r(i) + r(j)$$

where  $\vec{P}(i)$  is the position vector of disk  $i$ , and  $r(i)$  is the radius of disk  $i$ .

The normal unit vector  $\hat{n}$  is defined as the unit vector pointing from the center of disk  $i$  to the center of disk  $j$ , which is given by

$$\hat{n} = \frac{\vec{P}(j) - \vec{P}(i)}{d}$$

In the case of contact of particle  $i$  with a wall, the wall is considered as a particle with infinite radius and  $\hat{n}$  is the unit vector perpendicular to the wall and pointing away from the particle. The tangent unit vector  $\hat{t}$  is defined as the 90° clockwise rotation of  $\hat{n}$ , or

$$\hat{t} = (n_y, -n_x)$$

Here  $n_x$  and  $n_y$  are the  $x$  and  $y$  components of  $\hat{n}$ , respectively.

The normal relative velocity of disk  $j$  with respect to disk  $i$ ,  $\Delta V_n$ , is calculated as

$$\Delta V_n = [\vec{V}(j) - \vec{V}(i)] \cdot \hat{n}$$

where  $\vec{V}(i)$  is the velocity of particle  $i$ . The tangential relative velocity at the point of contact  $\Delta V_t$  results from both the relative translational velocity of the disks and their rotational velocities. This is given as

$$\Delta V_t = [\vec{V}(j) - \vec{V}(i)] \cdot \hat{t} + \omega(i) r(i) + \omega(j) r(j)$$

where  $\omega(i)$  is the rotational velocity of particle  $i$ . Figure 3-3 shows the contribution of the individual particle velocities to the relative normal and tangential velocities.

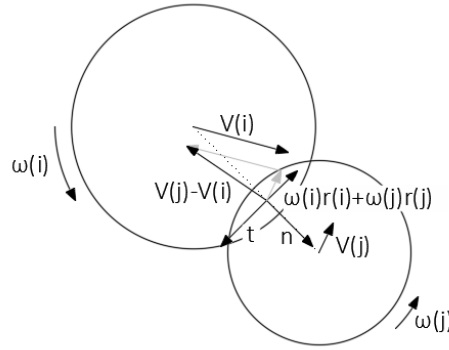


Figure 3-3 Contribution of particle velocities to relative normal and tangential velocities

During a time-step, the relative velocity causes a relative displacement increment. The components  $\Delta V_n dt$  and  $\Delta V_t dt$  are the displacements of disk  $j$  with respect to disk  $i$ , during the time-step, in the normal ( $\hat{n}$ ) and tangential ( $\hat{t}$ ) directions respectively. These displacements result in contact force increments which are calculated using the force-displacement law. Using a linear spring-dashpot model gives the contact force increments of

$$\Delta F_n = k_n \Delta V_n \Delta T$$

$$\Delta F_t = k_t \Delta V_t \Delta T$$

Here  $\Delta F_n$  and  $\Delta F_t$  are the contact force increments applied to disk  $j$  by disk  $i$ , respectively in the normal and tangential directions,  $k_n$  and  $k_t$  are respectively the normal and tangential spring stiffness representing the contact force, and  $\Delta T$  is the time increment.

The contact force at time  $T$ ,  $\vec{F}^T$ , has components in the normal and tangential directions which are  $\vec{F}^T \cdot \hat{n}$  and  $\vec{F}^T \cdot \hat{t}$  respectively. The contact force increments are added to the contact force components at the beginning of the time-step, in order to get the contact force components at the end of the time-step. This gives

$$F_n^{T+\Delta T} = \vec{F}^T \cdot \hat{n} + \Delta F_n$$

$$F_t^{T+\Delta T} = \vec{F}^T \cdot \hat{t} + \Delta F_t$$

Unlike the spring contact force which is developed incrementally, the contact damping force is independent of the time-step and is directly proportional to the relative velocity of contact. It is calculated using the contact damping coefficients  $\beta K_n$  and  $\beta K_t$  in the normal and tangential directions, respectively. These are given as

$$D_n = \beta K_n \Delta V_n$$

$$D_t = \beta K_t \Delta V_t$$

where  $D_n$  and  $D_t$  are respectively the normal and tangential contact damping forces. The damping coefficients are proportional to the spring stiffnesses  $K_n$  and  $K_t$  using the proportionality factor  $\beta$ . The tangential damping coefficient,  $\beta K_t$ , is not related to any experimentally measurable material property and is adjusted by comparison of simulation results with experiments (Poschel and Schwager 2005).

The total tangential force of the contact is then compared with the maximum allowable tangential force, which is the sum of sliding friction and cohesion. Sliding friction is calculated based on Coulomb law, using a friction coefficient of  $\tan(\varphi)$ , or

$$|F_t + D_t| \leq |F_n + D_n| \tan(\varphi) + c$$

where  $\varphi$  is the friction angle and  $c$  is cohesion.

Finally, the normal and tangential components of the contact forces are added together to get the total contact force vectors

$$\vec{F} = F_n \hat{n} + F_t \hat{t}$$

$$\vec{D} = D_n \hat{n} + D_t \hat{t}$$

where  $\vec{F}$  and  $\vec{D}$  are respectively the spring and damping contact forces applied to particle  $i$  due to contact with particle  $j$ . The contact torque is calculated from the tangential forces, as well and is given as

$$\tau(i, j) = -[F_t + D_t] r(i)$$

where  $\tau(j, i)$  is the torque applied to particle  $i$  due to contact with particle  $j$ .

The final contact forces and torque applied to disk  $j$  by disk  $i$  are therefore summarized as

$$\vec{F}(j, i) = -\vec{F}(i, j)$$

$$\vec{D}(j, i) = -\vec{D}(i, j)$$

$$\tau(j, i) = \tau(i, j) \frac{r(j)}{r(i)}$$

### 3.6 Energy Dissipation and Global Damping

A fraction of the kinetic energy of the system transforms into other forms of energy and ultimately to heat. This mainly occurs through friction and plastic deformation or viscoelasticity of the granular material. In DE simulations, energy is dissipated through friction, contact damping and global damping.

Sliding friction acts when the tangential contact force reaches a maximum value. Some studies, such as Zhou et al. (2002), have also used a rolling friction force that is proportional to the rotational velocity of the disk and the normal contact force.

While friction mechanisms affect individual particle dynamics and contact stability, the use of damping is necessary for the equilibrium of the system. Particulate systems would not be able to reach equilibrium, if no damping is included and instead, they would continue small elastic adjustments in position. Contact damping is provided by the normal and tangential dashpots and operates on the relative velocities of contacts. Global damping, also known as background friction, operates on the absolute translational and rotational velocities of the particles. Global damping force and torque are calculated as

$$\vec{F}_D = -\alpha m \vec{V}$$

$$\tau_D = -\alpha I \omega$$

where  $\alpha$  is the global damping coefficient,  $m$  is the mass of the particle, and  $I$  is the mass moment of inertia of the particle.

### 3.7 Application of Newton's Law of Motion

Once all the contact forces of the system are calculated, the resultant force and torque applied to each disk is calculated by summing all applied loads, including body force, contact forces and torques, and external loads.

$$m(i) \vec{\dot{V}}(i) = \sum_{j=1}^n [\vec{F}(i, j) + \vec{D}(i, j)] + \vec{F}_B(i) + \vec{F}_D(i) + \sum \vec{F}_E(i)$$

$$I(i) \dot{\omega}(i) = \sum_{j=1}^n \tau(i, j) + \tau_D(i)$$

where  $\vec{F}_B(i)$  is the body force and  $\sum \vec{F}_E(i)$  is the sum of the external forces applied to disk  $i$ .  $\sum_{j=1}^n [\vec{F}(i, j) + \vec{D}(i, j)]$  and  $\sum_{j=1}^n \tau(i, j)$  are respectively the sum of contact forces and torques applied to particle  $i$ . Based on the assumption that the particle acceleration is constant over a time-step, Newton's equations of motion are integrated to calculate the new particle velocities and

positions. The central finite difference method, used by Cundall and Strack (1979), is used for this time integration. The resultant force/torque is assumed to act on the disk from time  $T - \frac{\Delta T}{2}$  to  $T +$

$\frac{\Delta T}{2}$  and results in

$$\vec{V}^{T+\frac{\Delta T}{2}} = \vec{V}^{T-\frac{\Delta T}{2}} + \frac{\overline{\Sigma \vec{F}}^T}{m} \Delta T$$

$$\omega^{T+\frac{\Delta T}{2}} = \omega^{T-\frac{\Delta T}{2}} + \frac{\Sigma \tau^T}{I} \Delta T$$

Here  $\vec{V}$  and  $\omega$  in the global damping equation are evaluated as

$$\vec{V}^T = \frac{\vec{V}^{T-\frac{\Delta T}{2}} + \vec{V}^{T+\frac{\Delta T}{2}}}{2}$$

$$\omega^T = \frac{\omega^{T-\frac{\Delta T}{2}} + \omega^{T+\frac{\Delta T}{2}}}{2}$$

Substituting and solving for  $\vec{V}^{t+\frac{\Delta t}{2}}$  and  $\omega^{t+\frac{\Delta t}{2}}$  yields

$$\vec{V}^{T+\frac{dT}{2}} = \vec{V}^{T-\frac{dT}{2}} + \frac{\Sigma(\vec{F} + \vec{D}) + \vec{F}_B - \alpha m \frac{\vec{V}^{T-\frac{dT}{2}} + \vec{V}^{T+\frac{dT}{2}}}{2} + \vec{F}_E}{m} \Delta T$$

$$\omega^{T+\frac{dT}{2}} = \omega^{T-\frac{dT}{2}} + \frac{\Sigma \tau + -\alpha I \frac{\omega^{T-\frac{dT}{2}} + \omega^{T+\frac{dT}{2}}}{2}}{I} \Delta T$$

which is simplified to

$$\vec{V}^{T+\frac{\Delta T}{2}} = \frac{\left(1 - \frac{\alpha \Delta T}{2}\right) \vec{V}^{T-\frac{\Delta T}{2}} + \frac{\Sigma(\vec{F} + \vec{D}) + \vec{F}_B + \vec{F}_E}{m} \Delta T}{1 + \frac{\alpha \Delta T}{2}}$$

$$\omega^{T+\frac{\Delta T}{2}} = \frac{\left(1 - \frac{\alpha \Delta T}{2}\right) \omega^{T-\frac{\Delta T}{2}} + \frac{\Sigma \tau}{I} \Delta T}{1 + \frac{\alpha \Delta T}{2}}$$

These new velocities are used to update the position,  $\vec{P}$ , and angular orientation,  $\theta$ , of the disks

$$\vec{p}^{T+\Delta T} = \vec{p}^T + \vec{v}^{T+\frac{\Delta T}{2}} \Delta T$$

$$\theta^{T+\Delta T} = \theta^t + \omega^{T+\frac{\Delta T}{2}} \Delta T$$

This concludes the calculation cycle for the time step from time  $T$  to  $T + \Delta T$ . The new particle positions are then used for the next calculation cycle, starting with contact detection (See Figure 3-1). The time-stepping cycle continues until the simulation end time.

## 4. METHODS

### 4.1 Specimen Generation

The geometry of a particulate system is defined by the boundary conditions and the particle shape, size, orientation, and layout. Particle shape selection is the first step in setting up a DE model, since it governs the contact detection and contact force calculating algorithms. Once the appropriate boundary conditions and particle shapes are chosen, the next step is to place the particles in the domain to create the initial assemblies for simulation.

Most engineering problems that are studied using the DEM consist of dense particle packings. This is certainly the case in most geomechanics applications, where the particulate systems are initially in equilibrium under gravity and have relatively high densities. In order to obtain a dense packing, an initial arrangement of non-overlapping particles was generated and then was allowed to settle under gravitational force. This is true for all packings used in this study.

The initial arrangement of particles was created using a triangulation approach based on the method proposed by Cui and O'Sullivan (2003). Figure 4-1 shows the consecutive steps in creating a packing of 340 particles, using the triangulation method. A random number generator was used to produce random points within the domain. A mesh of triangles was then created using Delaunay triangulation of the set of random points. Delaunay triangulation of a set of points, is creating a triangular mesh by connecting the points such that no point is inside the circumcircle of any triangle in the mesh. This was carried out in MATLAB using the "DelaunayTri" command. A triangulation refinement was then carried out to break any large triangles into smaller ones so that the resulting particle radii was bound between 5 to 10 *mm*. Once the triangular mesh was finalized (Figure 4-1a), the first set of particles were inserted as the incircles of the triangles (Figure 4-1b).

Since the area surrounding the vertices are not covered by the incircles, a second set of particles were added at the vertices of the triangles, so that the radius of the disk was equal to the minimum clear distance to the adjacent incircles (Figure 4-1c). Lastly, a third set of particles were inserted in the remaining area of triangles between the incircles and the vertex circles (Figure 4-1d).

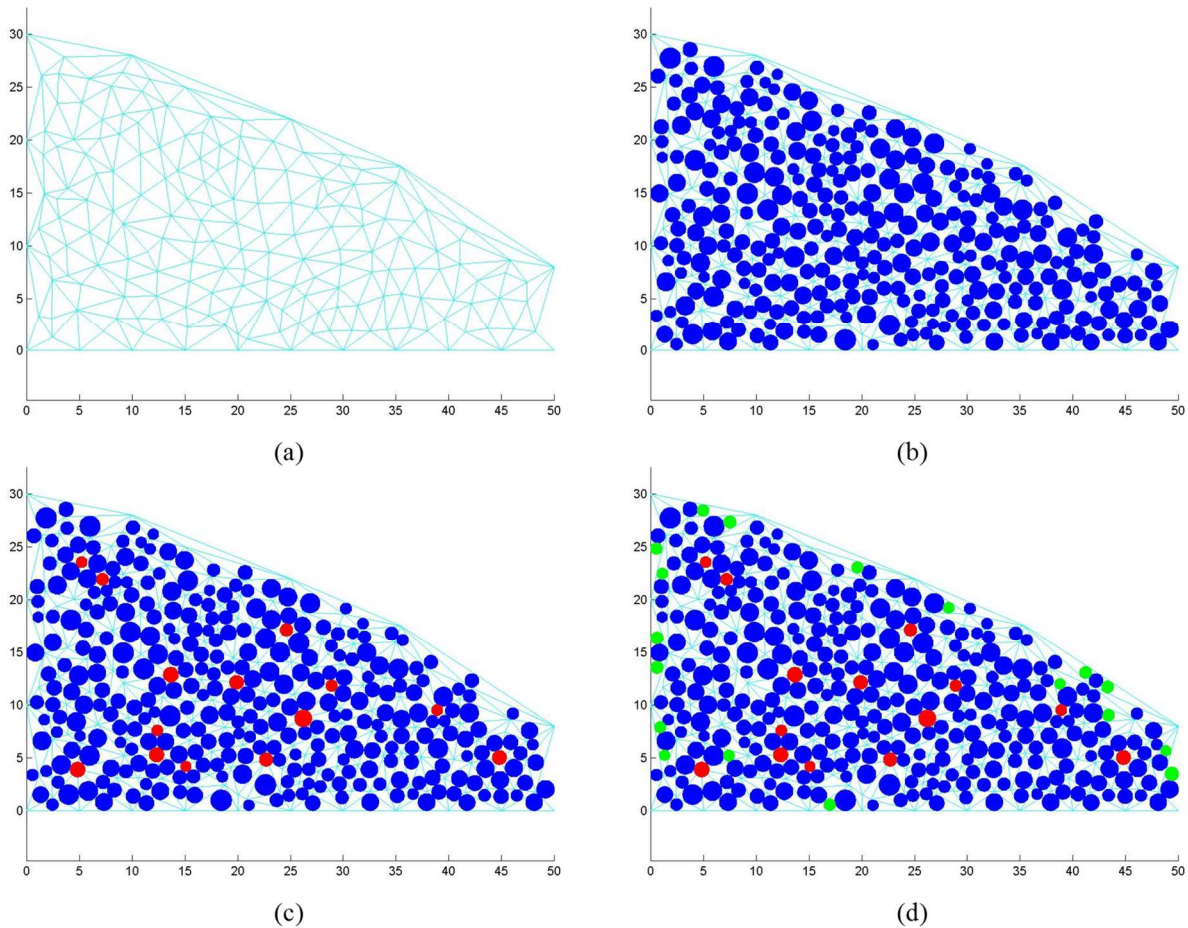


Figure 4-1 Specimen generation steps, (a) triangular mesh based on Delaunay triangulation of random points, (b) incircles of the triangles, (c) vertex infilling, (d) secondary incircles

Once the initial specimen of non-overlapping particles was finalized, a DE simulation was run to allow the particles to settle under gravity and form a stable heap. Figure 4-2 shows snapshots of the settling simulation for the specimen shown in Figure 4-1. The simulation was run for  $4 \times 10^6$  time-steps over a period of 4 seconds to allow complete stagnation of the system. The model parameters listed in Table 4-1 were used in the simulations.

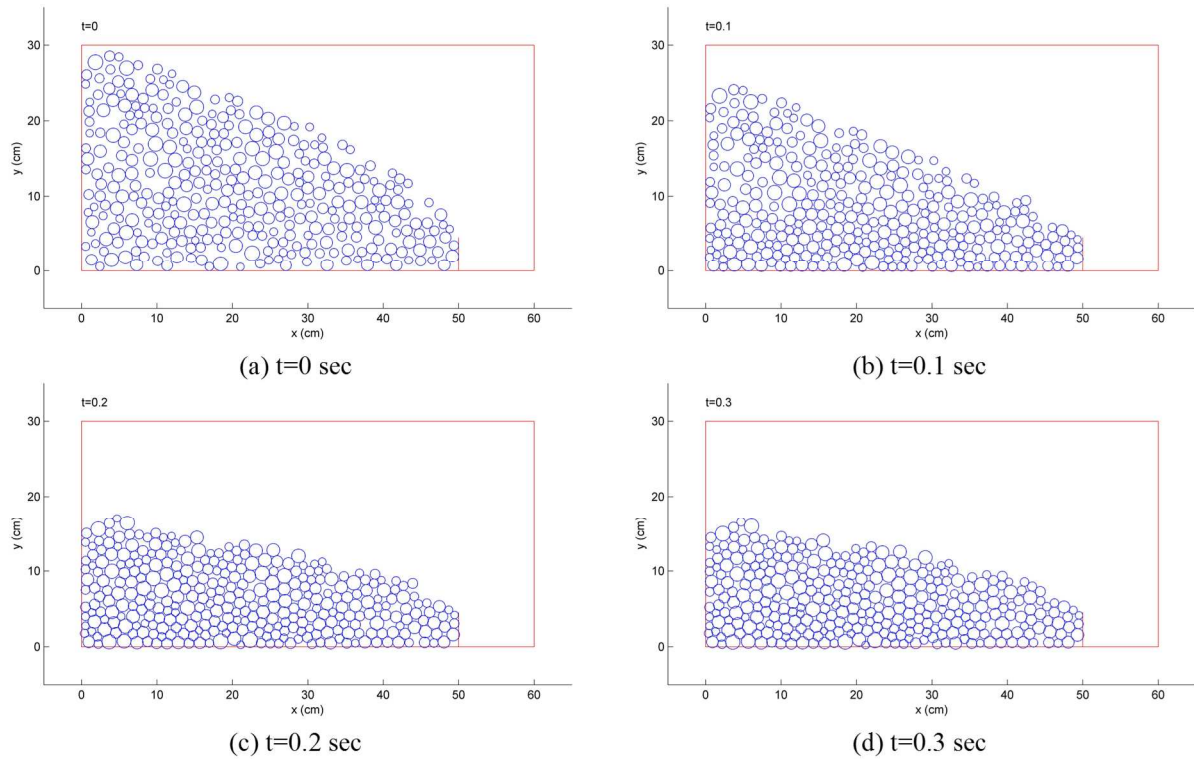


Figure 4-2 Settling of particles under gravity

The ten packings created using the triangulation approach with varying slopes and number of particles are shown in Figure 4-3 with the surface particles highlighted. The total number of particles in the packings range from 170 to 350 particles, and the slope of the packings range from  $7.6^\circ$  to  $16.5^\circ$ . The surface slope was calculated using a simple linear regression of the surface particle coordinates. These packings have random particle size distributions. Figure A-1 in Appendix A shows the corresponding particle size distribution for each packing.

To control for the effect of the particle size distribution in the behavior of the particulate systems, three packings with the same particle size distribution but also with varying slope were created. To generate these packings, the initial specimen used to produce the packing shown in Figure 4-3(j) was used and a body force in the positive  $x$  direction was added to the gravitational settling simulation to create the two other packings with lower slopes.

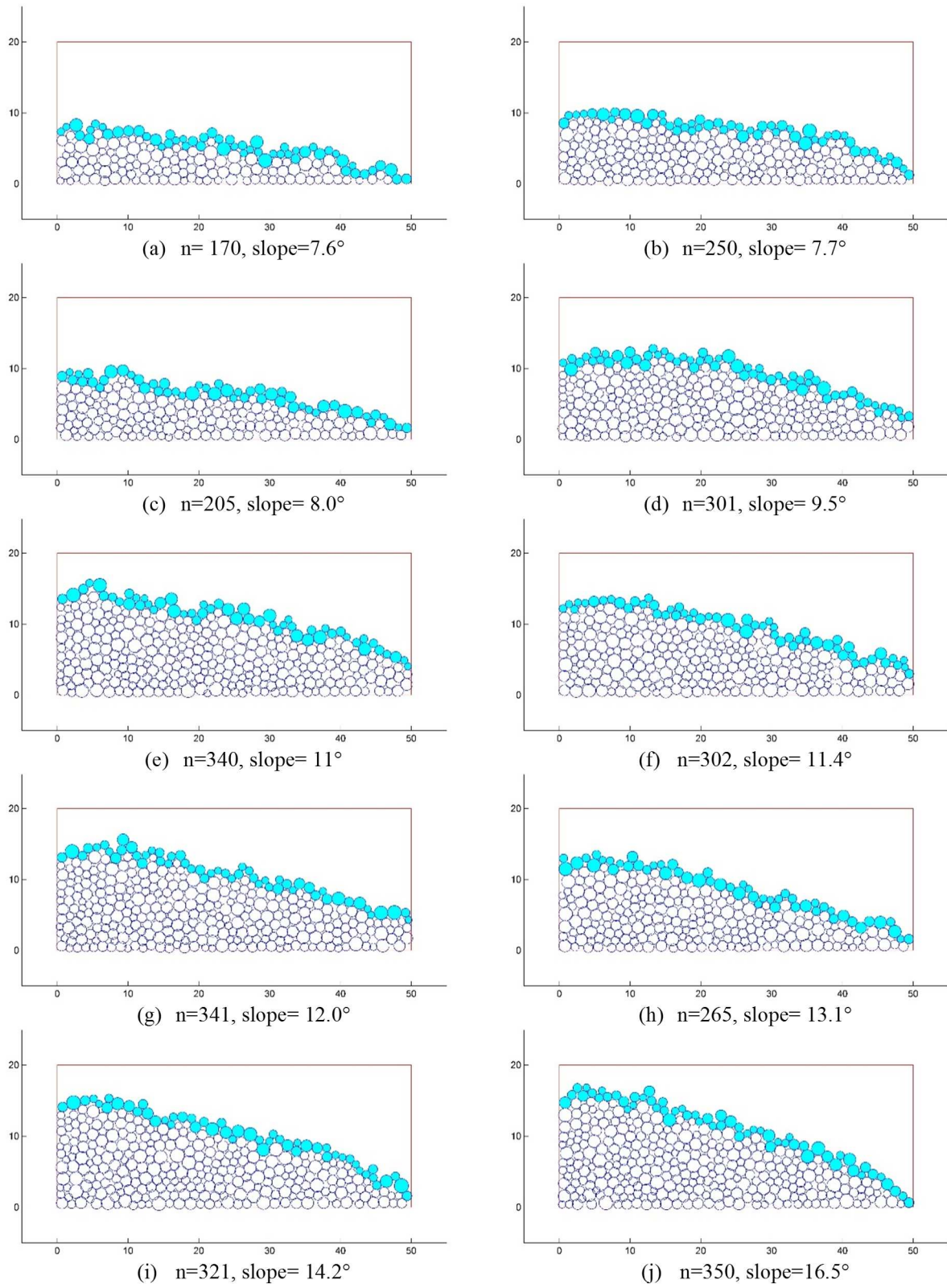


Figure 4-3 Particle packings with varying initial slopes, created using the triangulation method

The three packings with the same group of particles and the corresponding particle size distribution are shown in Figure4-4 and Figure4-5. The void ratio of the three packings were found to be about 0.12.

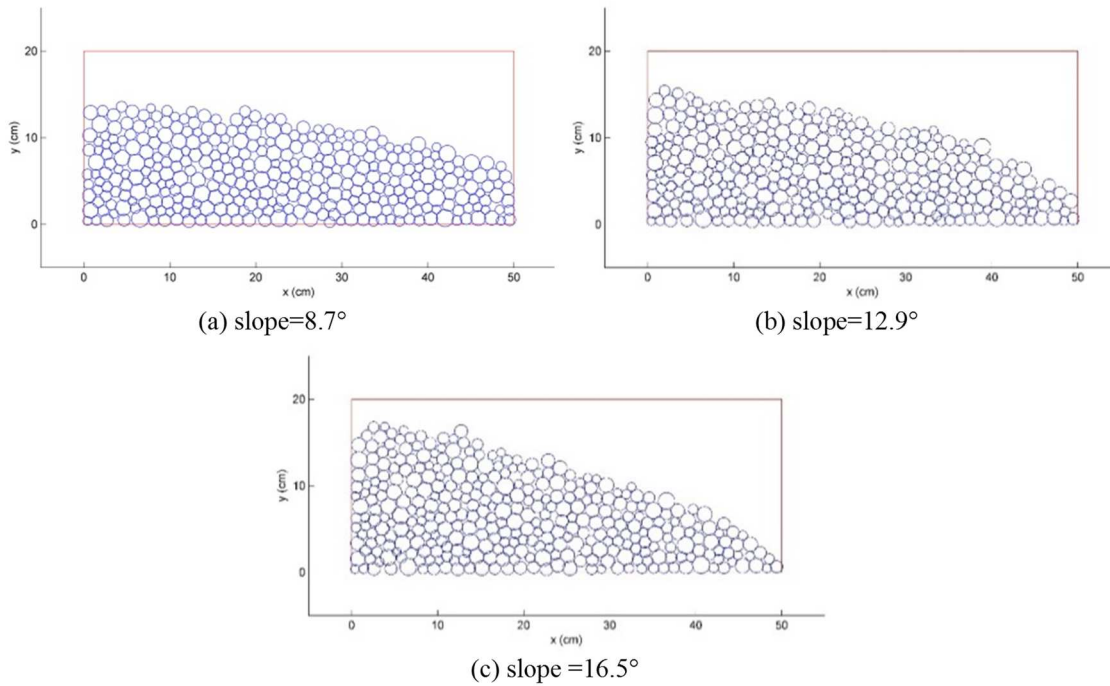


Figure 4-4 Packings with an identical particle group and varying slope

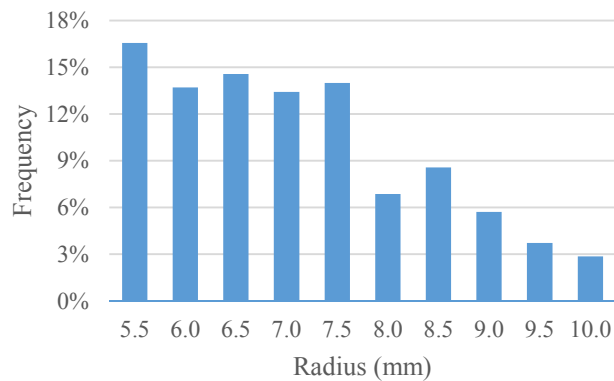


Figure 4-5 Particle size distribution of 350 particle packings

To create the 12.9° slope, a body force in the  $x$  direction was added to the particles above the line  $y = -0.24x + 12$ . The body force was linearly increased from zero to 0.25m(i)g during  $t = 0$  to  $t = 1$ sec and then linearly decreases back to zero during  $t = 1$  to  $t = 2$  sec. No body

force in the  $x$  direction was applied from  $t = 2$  to  $t = 4$  sec and the particles were allowed to redistribute internal forces and reach equilibrium. To create the  $8.7^\circ$  slope, the same approach was used, with the only differences being that the body force was applied to particles above the  $y = -0.28x + 14$  and the body force was increased up to  $0.57m(i)g$ . This method was arbitrarily selected and the body force in the  $x$  was adjusted from trial and error to create the desired slopes.

#### 4.2 Munjiza NBS Contact Detection

The Munjiza No-Binary Contact Search (i.e. Munjiza-NBS) algorithm, originally developed by Munjiza in 1995, was used to optimize RAM and CPU time requirements. The NBS contact detection method divides the space into rows and columns and as it proceeds row by row, it checks the particles of each cell with the ones in the neighboring cells for contact. The cells should be large enough to contain the largest particle, so that only particles from neighboring cells could have contact. The particles are mapped into each row using a loop in ascending order. This results in a descending list of the identification numbers of the particles in each row. These linked lists are concisely stored in only two arrays. An array  $A$  of size  $n_y$ , where  $n_y$  is the number of rows and array  $B$  of size  $n$ , which is the total number of the particles.

For element  $i$  in array  $A$ , the array contains the identification number of the last particle mapped into row  $i$ . Therefore, the fourth element of array  $A$ , for instance, contains the identification number of the last particle mapped into the fourth row, which would be the largest identification number of the particles in that row. If a row contains no particles, a negative value is stored in the corresponding element.

Element  $i$  of array  $B$  contains the identification number of the particle that comes next in the row lists after particle  $i$ . So if a row contains particles 5, 18 and 9, the list for that row would

be  $18 \rightarrow 9 \rightarrow 5$  and  $B(18) = 9$  and  $B(9) = 5$ . If particle  $i$  is the one with the smallest identification number in a row, it would be the last particle in the row list and a negative value is assigned to  $B(i)$ .

Figure 4-6 demonstrates the method with an example. Figure 4-6a shows a domain, which is divided into 5 rows and 5 columns of cells, and the 10 particles that are within the domain. For each row, the descending list of the identification numbers of the particles within the row is written. Figure 4-6b shows the arrays that store the row lists and also shows, as an example, how the list for the second row, can be obtained from the arrays.

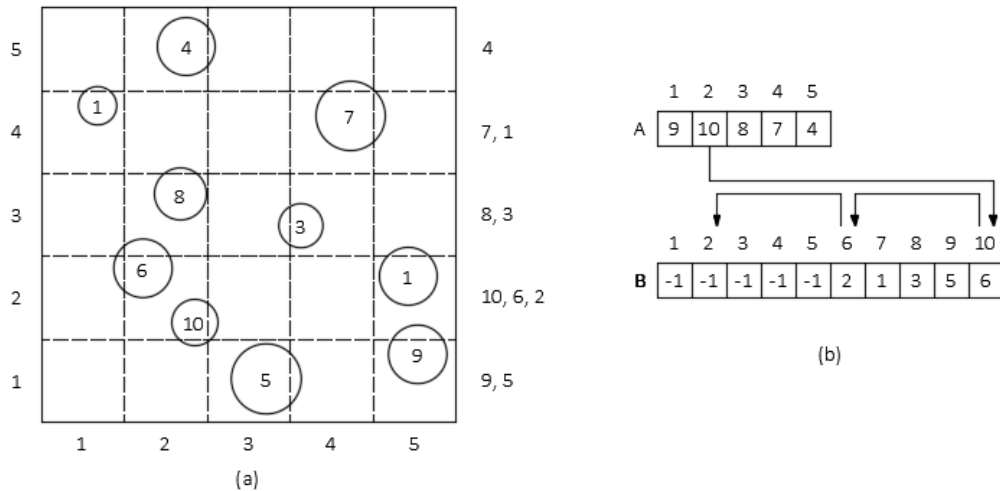


Figure 4-6 Example of particle mapping using the NBS method, (a) for each row of cells, the ascending list of the particle numbers is created (b) the lists are stored in arrays A and B as linked lists

After mapping particles into rows, particles in each row are mapped into individual cells using a similar approach. To be able to check contact of discrete elements in neighboring rows, two adjacent rows are mapped into cells. Finally, particles mapped into each cell are checked for contact with the ones mapped into the same and neighboring cells.

### 4.3 Surface Reinforcement

Vegetation has been found to improve slope stability and reduce erosion, through mechanical and hydrological effects. Mechanically, the interaction of the soil and the roots results

in a composite behavior, reinforcing the soil, and increasing its strength (Cazzuffi, Cardile and Gioffrè 2014). Reinforcements of the slope surface, in the form of springs connecting surface particles to each other or to particles under the surface, were implemented to represent the effect of vegetation roots.

Four reinforcing patterns were modeled to investigate the effect of such reinforcing on flow-generated displacements of granular packings: 1) net reinforcing pattern, 2) 25% shallow reinforcing, 3) 25% deep reinforcing and 4) 50% shallow reinforcing. The net reinforcing pattern connects neighboring surface particles of a packing with reinforcing springs. The 25% and the 50% shallow reinforcing patterns, respectively connect 25% and 50% of the surface particles to particles beneath the surface. These reinforcing elements are shallow and do not extend deep into the packing whereas the 25% deep reinforcing pattern connects the same surface particles to deeper particles in the packing. The reinforcement is distributed evenly throughout the surface.

The method used for the calculation of the forces applied by the reinforcement elements was very similar to the inter-particle normal contact force calculation. The reinforcement forces are zero at the beginning of the simulation and develop over time-steps incrementally. The reinforcement forces are part of the external forces applied to the particles and contribute to  $\sum \vec{F}_E$  (See section 3.7). They are assumed to be applied to the centers of the disks and therefore do not cause torque. The stiffness of the reinforcing springs was selected to be  $0.2 K_n$ . The reinforcing elements were set to remain active as long as the displacements of the connected particles were minimal and to break off if the absolute velocity of either of the connected particles exceeded  $2 \text{ cm/sec}$ . This limit was arbitrarily selected and was adjusted based on simulation results so that the reinforcement becomes inactive when substantial movements occurs.

#### 4.4 Flow-Generated Forces

The force applied by runoff to the soil particles on the surface of a slope is influenced by a variety of factors, such as the geometry of the slope, runoff velocity, density and compactness of the soil, exposure of each particle to flow, etc. Accounting for the effect of all such factors was beyond the scope of this study, and therefore several simplifying assumptions were made in the modeling of the flow-generated forces.

To account for the fact that the larger particles typically have a larger surface exposed to flow, it was assumed that the drag force applied to surface particles is proportional to the radius of the particles. It was presumed that the force applied by runoff to the particles is zero initially and then increases linearly for a period of 1 second to a maximum value of  $H \times r(i)$  Newtons. The coefficient  $H$  was selected to be 3.2, 4.0 and 4.4  $N/m$  in the various simulations, that correspond to flow velocities of 0.65, 0.73, and 0.76  $m/sec$ . The drag equation

$$F_D = \frac{1}{2} \rho V^2 C_d A$$

was used to calculate the flow velocity corresponding to the different  $H$  values, where  $F_d = Hr$  is the drag force applied to a particle,  $\rho = 1000 \text{ Kg}/m^3$  is the density of water,  $V$  is the velocity of flow,  $C_d$  is the drag coefficient and is assumed to be 0.75, and  $A = 2r$  is the projected particle surface area perpendicular to flow. The drag coefficient was selected based on the drag coefficient of 0.5 for a sphere and 0.8 for a cube (Hoerner 1965).

It was also assumed that the surface particles are submerged in water and that the buoyancy force will counteract the downward component of the drag force applied to these particles. Therefore, the drag force was only applied in the horizontal direction to the surface particles.

## 4.5 Model Properties

The properties listed in Table 4-1 were used in the simulations that follow, unless noted otherwise. Soil particle density of  $2.56 \text{ g/cm}^3 = 2560 \text{ Kg/m}^3$  was assumed. The normal contact spring stiffness  $K_n = 2.0 \text{ N/cm}$  was selected in order to limit the static deflection of the largest particle with  $r = 10 \text{ mm}$  under its self-weight to  $(4 \times 10^{-4})r$ . The tangential contact spring stiffness,  $K_t = 0.2 \text{ N/cm}$ , was selected as a fraction of  $K_n$ , and adjusted after iterations to create realistic rotational movement of particles in various simulations. Friction angle  $\theta = 35^\circ$  and cohesion  $c = 0$  was selected to represent cohesion-less dry sand. Global and contact damping constants,  $\alpha$  and  $\beta$ , were adjusted using trial and error, to achieve realistic damping behavior. (See section 5.1)

Table 4-1 Model properties

Variable	Symbol	Value
Particle density	$\rho$	$2,560 \text{ Kg/m}^3$
Normal contact spring stiffness	$K_n$	$2.0 \text{ N/cm}$
Tangential contact spring stiffness	$K_t$	$0.2 \text{ N/cm}$
Friction angle	$\varphi$	$35^\circ$
Cohesion	$c$	$0.0$
Global damping constant	$\alpha$	$3.0$
Contact damping constant	$\beta$	$0.15$
Time increment	$dT$	$10^{-6} \text{ sec}$

## 5. RESULTS AND DISCUSSION

### 5.1 DEM Validation

Benchmark simulations were carried out to investigate the validity of the developed discrete element code and the accuracy of the contact model. The collision of a particle with a rigid wall and the collision of two particles were both simulated. The analytical solutions to the equations governing the particle dynamics were compared with the results of the DE model. Accuracy of results, stability of the simulations and energy dissipation in the system were investigated and considered in selection of the appropriate time-step, contact force parameters and damping coefficients.

#### 5.1.1 Collision of a Particle with a Rigid Wall

The first simulation studied is the settling of a particle on a rigid surface under its weight. The particle is initially merely touching the rigid surface underneath and has no initial velocity. Although static equilibrium cannot be achieved in a DE model, if parameters such as the time-step, the spring stiffness, and the damping coefficients for the contact force model are set correctly, a quasi-static equilibrium can be attained. As the simulation begins, the particle will slowly move downward in each time-step under the gravitational acceleration. The rigid surface causes the particle to deform, which is visualized as an overlap of the particle and the wall and as a result, a contact force is developed between the rigid surface and the particle.

Figure 5-1 schematically shows all the contact and global damping force models that apply to a particle-wall collision. In this case, since the initial velocity of the particle is zero and the movement due to gravity is only in the vertical direction, the tangential forces and the global rotational damping force are zero.

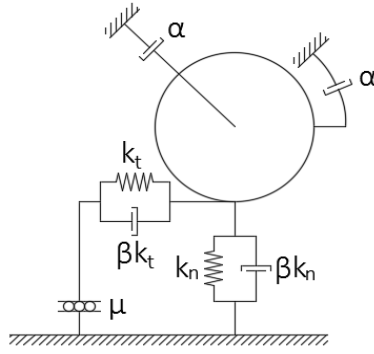


Figure 5-1 Force models for a particle-wall collision

When there is no global damping, the only external force applied to the particle is the normal contact force applied by the rigid surface. If this is modeled as a linear spring, the contact force is proportional to the deformation,  $\Delta$ , which is the overlap developed between the particle boundary and the rigid surface, calculated as

$$\Delta = \frac{mg}{k_n} - y(t)$$

where  $y$  is measured from the position of static equilibrium, positive in the upward direction (Figure 5-2). Applying Newton's second law, we have

$$m\ddot{y} = -mg + k_n\Delta$$

which simplifies to the equation of motion for an un-damped spring-mass system.

$$m\ddot{y} = -k_n y$$

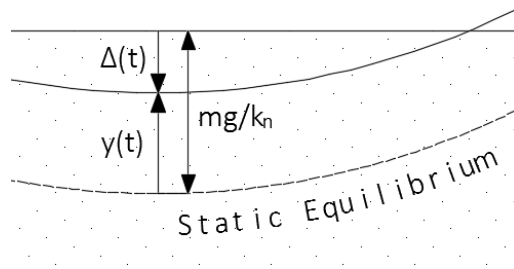


Figure 5-2  $\Delta(t)$  and  $y(t)$

This is a homogenous second-order differential equation that subject to the initial conditions, gives the solution

$$y(t) = \frac{mg}{k_n} \cos(\omega t)$$

which indicates a harmonic motion with the natural circular frequency of

$$\omega = \sqrt{\frac{k_n}{m}}$$

The particle moves down into the surface until the contact force reaches its maximum value and the particle is pushed back up to its initial position. Since there is no energy dissipation the oscillations go on indefinitely.

However, if the contact force is modeled as a linear spring-dashpot model, the oscillations will dissipate until the particle reaches a quasi-static equilibrium in which the contact force is almost equal to the weight of the particle and the velocity of the particle is almost zero. In this case the equation of motion is

$$m\ddot{y} = -k_n y - \beta k_n \dot{y}$$

which has three different solutions based on the value of the damping coefficient. If  $\beta k_n$  is smaller than the critical damping coefficient of

$$c_c = 2\sqrt{k_n m}$$

the system is under-damped and will experience a declining oscillatory motion with the damped circular frequency of  $\sqrt{1 - \zeta^2} \omega$ . The solution to the equation of motion, subject to the initial conditions, is

$$y(t) = \frac{mg}{k_n} e^{-\zeta \omega t} \left[ \frac{\zeta}{\sqrt{1 - \zeta^2}} \sin\left(\sqrt{1 - \zeta^2} \omega t\right) + \cos\left(\sqrt{1 - \zeta^2} \omega t\right) \right]$$

where

$$\zeta = \frac{\beta k_n}{c_c}$$

is the damping ratio. However, if the system is over-damped and  $\beta k_n > c_c$ , the solution is

$$y(t) = \frac{mg}{k_n} \left[ \frac{\zeta + \sqrt{\zeta^2 - 1}}{2\sqrt{\zeta^2 - 1}} e^{(-\zeta + \sqrt{\zeta^2 - 1})\omega t} - \frac{\zeta - \sqrt{\zeta^2 - 1}}{2\sqrt{\zeta^2 - 1}} e^{(-\zeta - \sqrt{\zeta^2 - 1})\omega t} \right]$$

which indicates non-oscillatory motion.

In the following discussion, for all simulations a particle with  $r = 7.5 \text{ mm}$  was used to represent the median particle size used in the packing simulations. The weight of the particle was  $4.44 \times 10^{-2} \text{ N}$  and a normal spring stiffness of  $K_n = 2 \text{ N/cm}$  was used. The static equilibrium deformation was  $mg/K_n = 2.22 \times 10^{-2} \text{ cm} = 0.03 r$  and a time step of  $10^{-4} \text{ sec}$  was used. The critical damping coefficient was  $\beta = 0.095$ . Data points for every 0.02 sec were used to create the figures.

Figure 5-3 shows particle deformation,  $\Delta$ , over time for the different values of contact damping coefficient,  $\beta$ . As  $\beta$  is increased, more energy is dissipated in each oscillation, the amplitude of the motion is decreased and the system reaches the quasi-static equilibrium over a shorter period of time. Once the system was over-damped,  $\beta = 0.1$ , the oscillatory behavior disappeared and the particle settled into its quasi-static equilibrium within about 0.5 seconds.

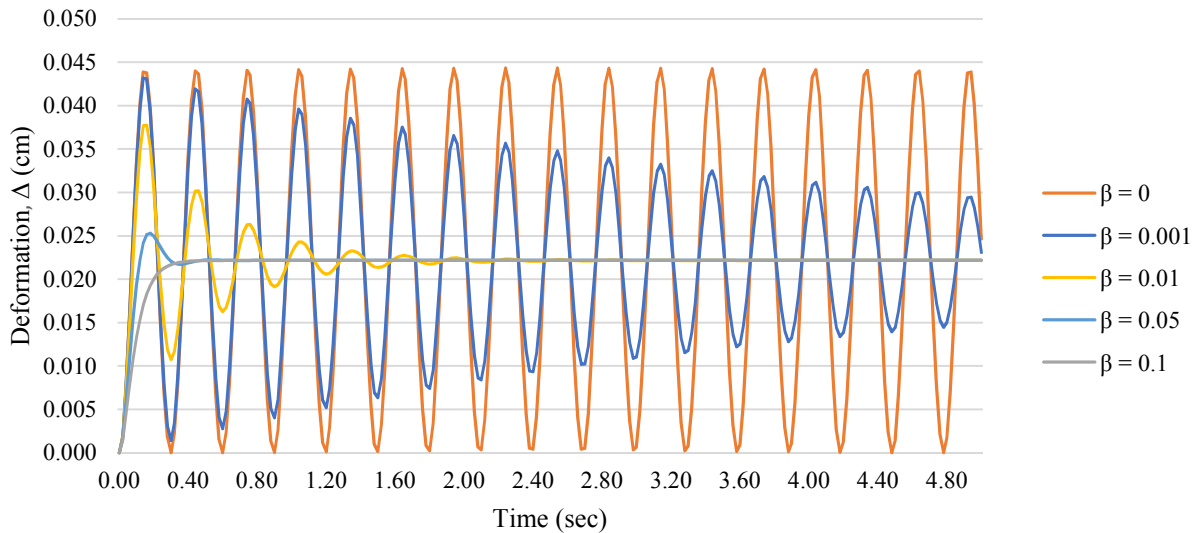


Figure 5-3 Effect of contact damping on the particle-wall collision

Figure 5-4 shows the percent error of the simulation results over time, for the case of no global damping ( $\alpha = 0$ ) and under-damped spring-dashpot model with  $\beta = 0.01$ . Figure 5-5 shows the percent error of the simulation results over time, for the case of no global damping ( $\alpha = 0$ ) and over-damped spring-dashpot model ( $\beta = 0.1$ ). The percent error was calculated as

$$\% \text{ error}(t) = \frac{\Delta_{\text{exact}}(t) - \Delta_{\text{simulation}}(t)}{\Delta_{\text{exact}}(t)} \times 100$$

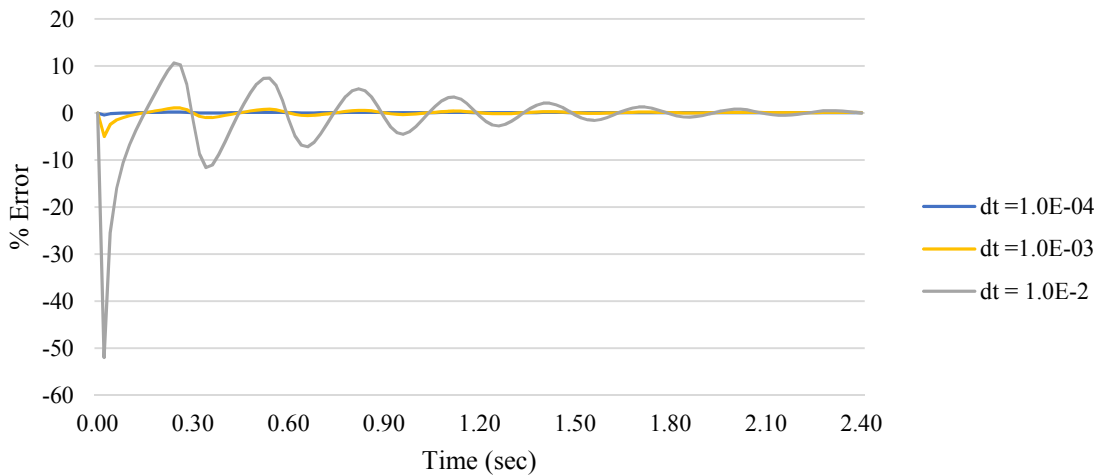


Figure 5-4 Effect of time-step on simulation error for  $\alpha=0$  and  $\beta=0.01$

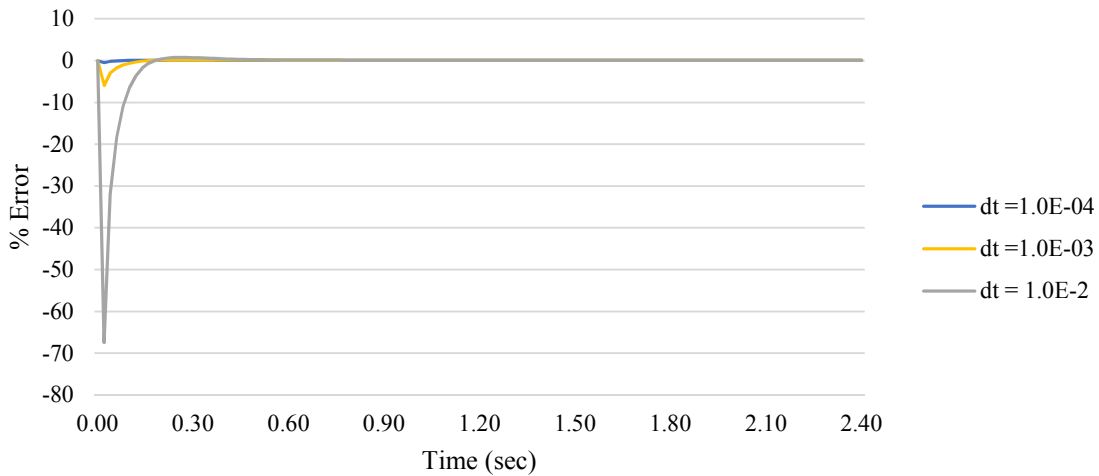


Figure 5-5 Effect of time-step on simulation error for  $\alpha=0$  and  $\beta=0.1$

The simulations were carried out using three different time-step values. In all cases, the percent error at the beginning of the simulation is larger and decreases as the simulation goes on. It is shown that for each time-step value, the percent error approaches zero in a shorter period of

time when  $\beta$  is larger. It is also shown that in both cases of under-damped and over-damped system, the percent error is reduced when smaller time-steps are used.

When global damping is applied, the simulation results cannot be directly compared with analytical solutions. This is due to the way global damping is integrated in the DEM algorithm. Global damping does not apply an external force on the particle, and is only embedded in the integration of the equation of motion. This was explained in more detail in section 3.7. Therefore, once global damping is applied, the equation of motion can only be solved numerically.

Figure 5-6 shows the effect of global damping on particle deformation for a simple spring-mass system with no contact damping. The global damping acted similarly to the contact damping and reduced the amplitude of the motion until it was negligible and the oscillatory behavior was eliminated (see Figure5-3). However, unlike contact damping, global damping did not affect the frequency of the oscillations and could not produce non-oscillatory motion.

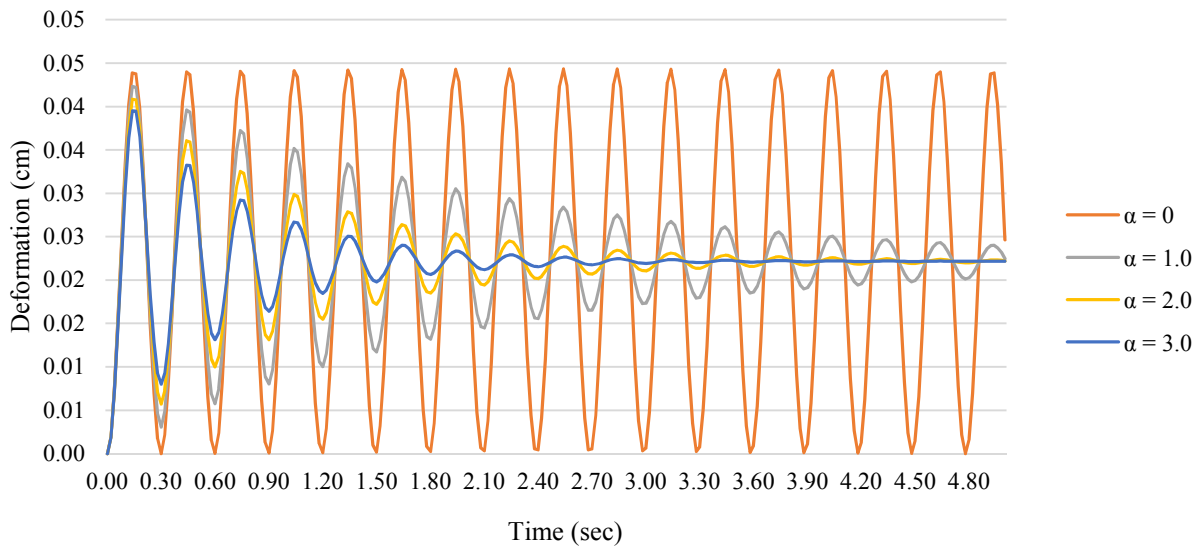


Figure 5-6 Effect of global damping on the particle-wall collision without contact damping

Figure 5-7 shows the effect of global damping on particle deformation for spring-dashpot systems. The contribution of global damping becomes less significant when the contact damping is increased.

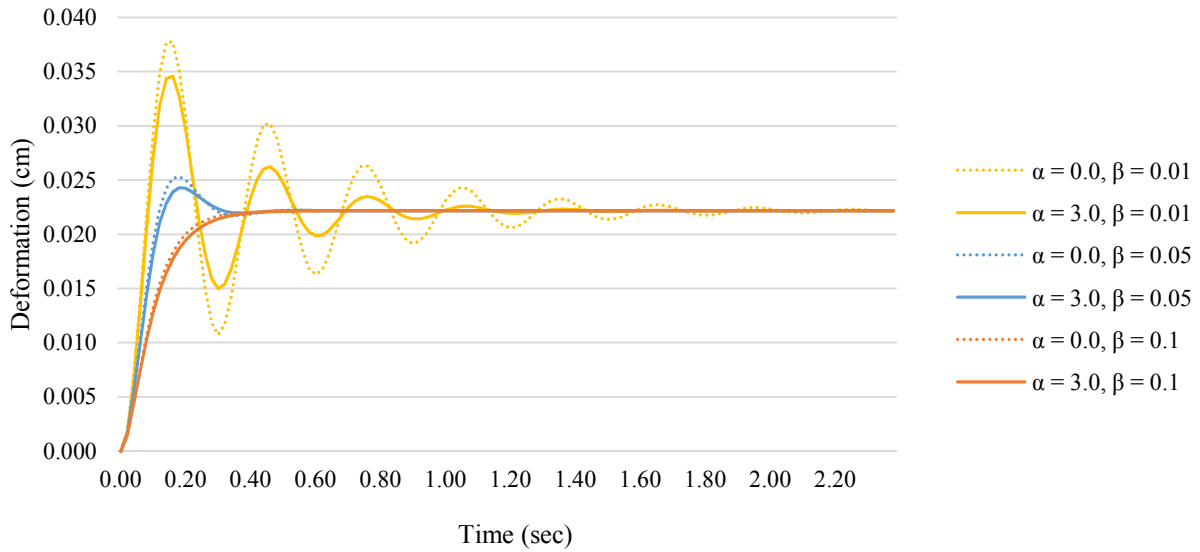


Figure 5-7 Effect of global damping on the particle-wall collision with contact damping

### 5.1.2 Collision of Two Particles

In this section, collision of two particles moving on a horizontal surface is simulated. Particle velocities are studied and compared with analytical solutions.

Figure 5-8 shows the contact and global damping force models that apply to a particle-particle collision. To compare simulation results with analytical solutions, a normal collision was simulated, so that tangential forces were zero, and global damping was disabled. It is assumed that the particles are on a frictionless horizontal surface, therefore the only force applied to each particle in the normal contact force.

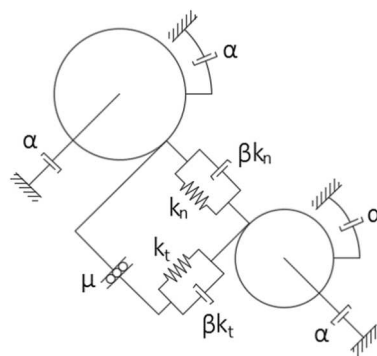


Figure 5-8 Force models for a particle-particle collision

The first particle, with the initial velocity of  $\dot{x}_1(0) = 1 \text{ cm/s}$  and  $\dot{y}_1(0) = 0 \text{ cm/s}$  hits the second particle which is stationary, along the x direction. Applying Newton's law of motion, we have

$$m\ddot{x}_1 = -k_n\ddot{\Delta} - \beta k_n\dot{\Delta}$$

$$m\ddot{x}_2 = -k_n\ddot{\Delta} - \beta k_n\dot{\Delta}$$

where  $\Delta$  is the overlap developed between the particles. The relationship between  $x_1$ ,  $x_2$  and  $\Delta$  is

$$x_2 - x_1 - 2r + \Delta = 0$$

Substituting the equations of motion into the former equation, we have

$$m\ddot{\Delta} = -2k_n\Delta - 2\beta k_n\dot{\Delta}$$

With the initial conditions of  $\Delta(0) = 0$  and  $\dot{\Delta}(0) = 1$ , the solution is

$$\Delta(t) = \frac{1}{\omega} \sin(\omega t) \quad \text{if } \beta = 0$$

$$\Delta(t) = e^{-\zeta\omega t} \frac{1}{\omega\sqrt{1-\zeta^2}} \sin\left(\sqrt{1-\zeta^2}\omega t\right) \quad \text{if } \zeta < 1$$

$$\Delta(t) = \frac{1}{2\omega\sqrt{\zeta^2-1}} \left( e^{(-\zeta+\sqrt{\zeta^2-1})\omega t} - e^{(-\zeta-\sqrt{\zeta^2-1})\omega t} \right) \quad \text{if } \zeta > 1$$

where

$$\omega = \sqrt{\frac{2k_n}{m}}$$

$$\zeta = \frac{\beta k_n}{\sqrt{2k_n m}}$$

Substituting into the equation of motion and solving for  $x_1(t)$ , with the initial conditions of  $x_1(0) = 0$  and  $\dot{x}_1(0) = 1$ ,

$$\dot{x}_1(t) = \frac{1}{2} \cos(\omega t) + \frac{1}{2} \quad \text{if } \beta = 0$$

$$\dot{x}_1(t) = \frac{1}{2} \left[ e^{-\zeta\omega t} \cos(\sqrt{1-\zeta^2} \omega t) - \frac{\zeta}{2\sqrt{1-\zeta^2}} e^{-\zeta\omega t} \sin(\sqrt{1-\zeta^2} \omega t) \right] + \frac{1}{2} \quad \text{if } \zeta < 1$$

$$\dot{x}_1(t) = \frac{1}{4} \left[ \left(1 + \frac{\zeta}{\sqrt{\zeta^2-1}}\right) e^{-(\zeta+\sqrt{\zeta^2-1})\omega t} + \left(1 - \frac{\zeta}{\sqrt{\zeta^2-1}}\right) e^{-(\zeta-\sqrt{\zeta^2-1})\omega t} \right] + \frac{1}{2} \quad \text{if } \zeta > 1$$

Figure 5-9 shows the percent error of the simulation results for  $\dot{x}_1$  over time for various contact damping coefficients. It is shown that for the un-damped spring-mass system, the error increases during the collision, which could be due to accumulation of error. On the other hand, for the under-damped spring-dashpot systems, the error increases to a maximum value of 3% for  $\beta = 0.001$  and 8% for  $\beta = 0.01$  and then decreases to about 1%. The final error in calculating particle velocity after collision decreased from about 6% to 0.01% as the damping coefficient,  $\beta$ , increased from zero to 0.1. The error was the smallest when the contact force was modeled as an over-damped spring-dashpot model, and the difference between the simulation results and the analytical solution was negligible, less than 0.16%, throughout the collision.

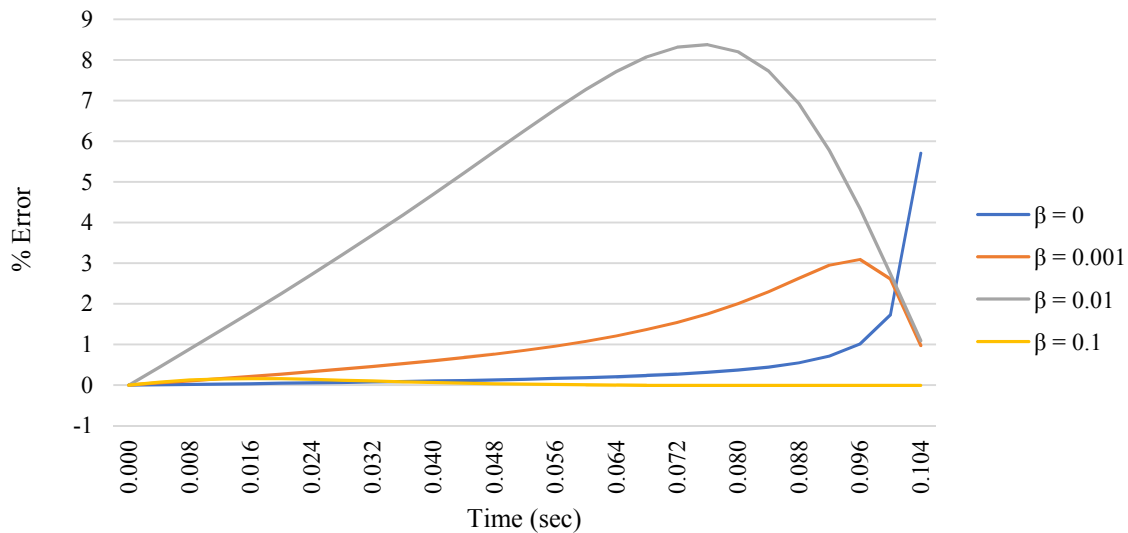


Figure 5-9 Simulation error in calculation of  $\dot{x}_1$ , for various contact damping coefficients

Figure 5-10 shows the simulation results for the velocity of the two particles over time. It shows how momentum is transferred from the first to the second particle during the collision. The

simulations were carried out using various contact damping coefficients. When there is no contact damping, the momentum of the first particle is completely transferred to the second particle. When damping is applied, part of the momentum is transferred to the second particle, and the first particle retains part of its velocity. If the contact model is over-damped, the two particles act as a single joint particle and proceed with the same velocity after the collision. The figure also shows that the duration of contact is increased as  $\beta$  is increased.

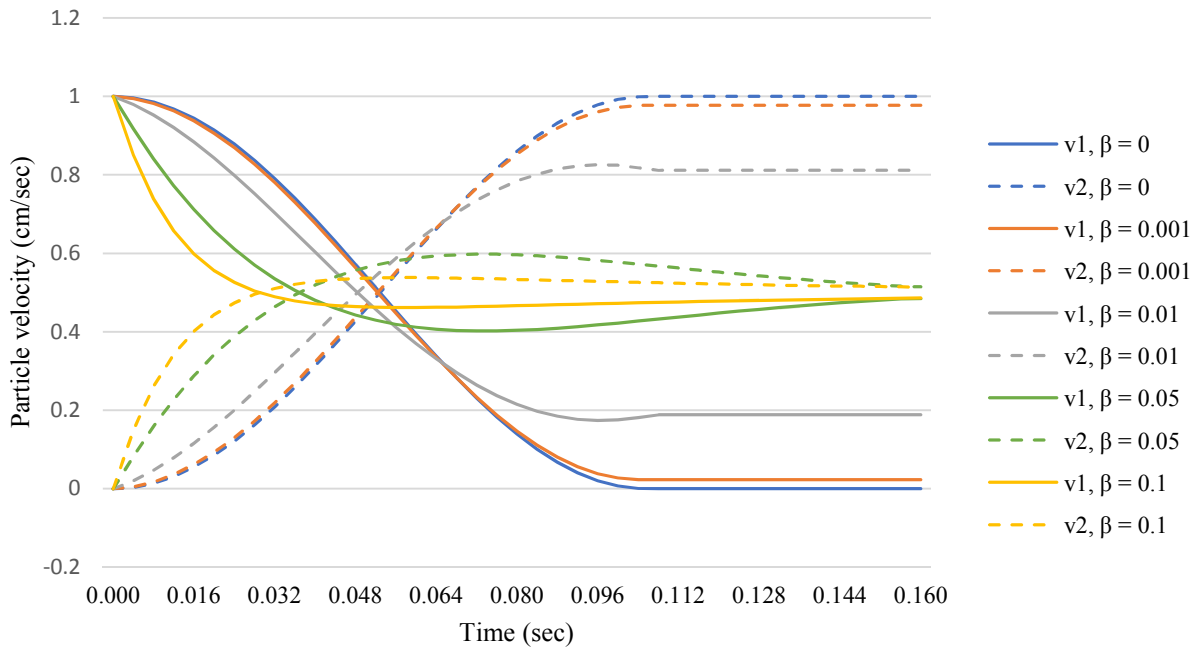


Figure 5-10 Particle velocities during collision for various contact damping coefficients

Figures 5-11 shows the percent change in the momentum of the system after collision, for the different contact damping coefficients. Change in momentum of the system was negligible in all simulations, less than  $10^{-12}\%$ . Figure 5-12 shows the percent change in kinetic energy of the system, which increased from 0% to about 50% as the contact damping coefficient,  $\beta$ , was increased from zero to 0.05. The dissipation of the kinetic energy of the system did not change as  $\beta$  increased from 0.05 to 0.1.

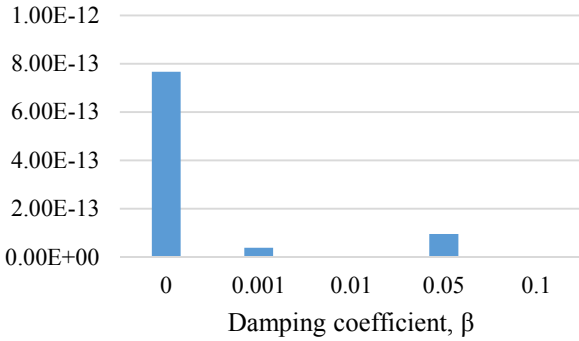


Figure 5-11 Percent change in momentum of the system

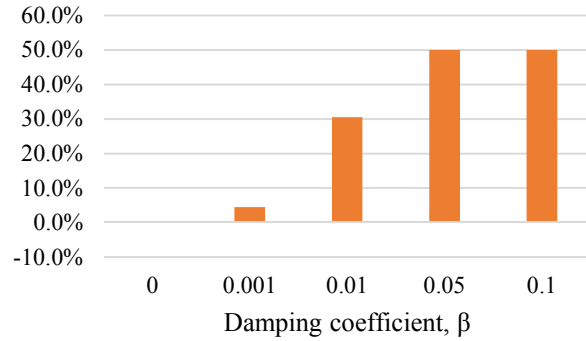


Figure 5-12 Percent change in kinetic energy of the system

## 5.2 Parametric Study

Numerous simulations were carried out to study the effect of the key parameters on flow-generated displacements of reinforced granular packings. The key parameters investigated were the initial slope of the particle packing, the quantity and type of surface reinforcements and the magnitude of the applied flow-generated forces. The following discussions explain how the effect of each parameter was measured and the results obtained.

### 5.2.1 Packings with Various Particle Size Distributions

To investigate the effect of the initial slope of granular packings on flow-generated displacements, packings with different surface slopes were created and exposed to the same flow-generated surface forces. Ten packing samples with slopes ranging from  $7.6^\circ$  to  $16.5^\circ$  degrees were modeled. Figure 4-3 shows the unreinforced packings, with the surface particles highlighted before flow-generated forces are applied. The model properties listed in Table 4-1 were used here and a reinforcing spring stiffness of  $k_r = 0.2k_n$  was used for all the simulations. The applied flow-generated forces increased linearly from 0 to a maximum value of  $4r(i)$  Newtons, from  $t = 0$  to  $t = 1$  sec and was kept constant from  $t = 2$  to  $t = 3$  sec. (See section 4.4)

Figure 5-13 shows the average flow-generated displacement of surface particles for each packing during the simulation. The average surface particle displacement at time  $T$ ,  $\overline{\Delta S}^T$ , was calculated using

$$\overline{\Delta S}^T = \overline{\Delta S}^{T-\Delta T} + \frac{1}{n} \sum_{i=1}^n \sqrt{\Delta x(i)^2 + \Delta y(i)^2}$$

where  $\overline{\Delta S}^{T-\Delta T}$  is the average surface particle displacement of the previous time-step and  $\Delta x(i)$  and  $\Delta y(i)$  are the displacements of particle  $i$  during the time-step in the  $x$  and  $y$  direction, respectively.

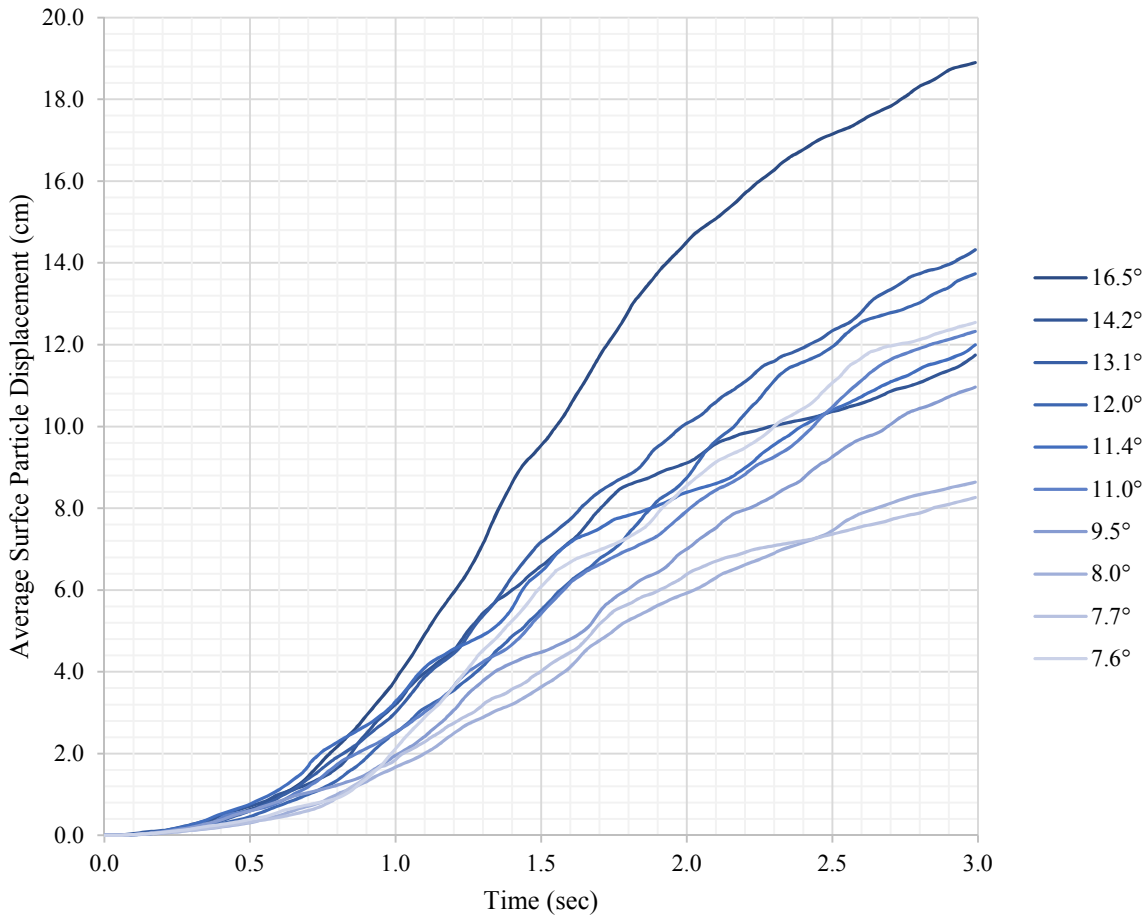


Figure 5-13 Average flow-generated displacement of surface particles of unreinforced packings

Figure 5-14 shows the average flow-generated displacement of surface particles for each packing at  $t = 3 \text{ sec}$ .

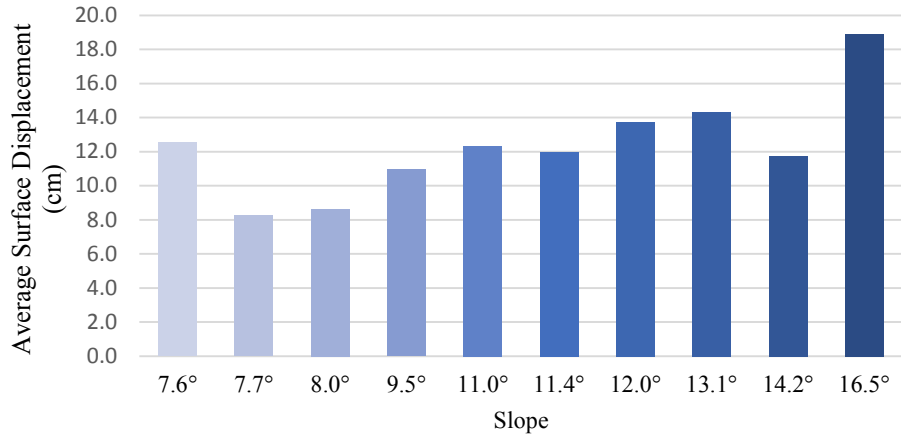


Figure 5-14 Average flow-generated displacement of surface particles at t=3sec

Figure 5-15 show the average flow generated displacement of surface particles during the simulation for the unreinforced packings with the same particle size distribution.

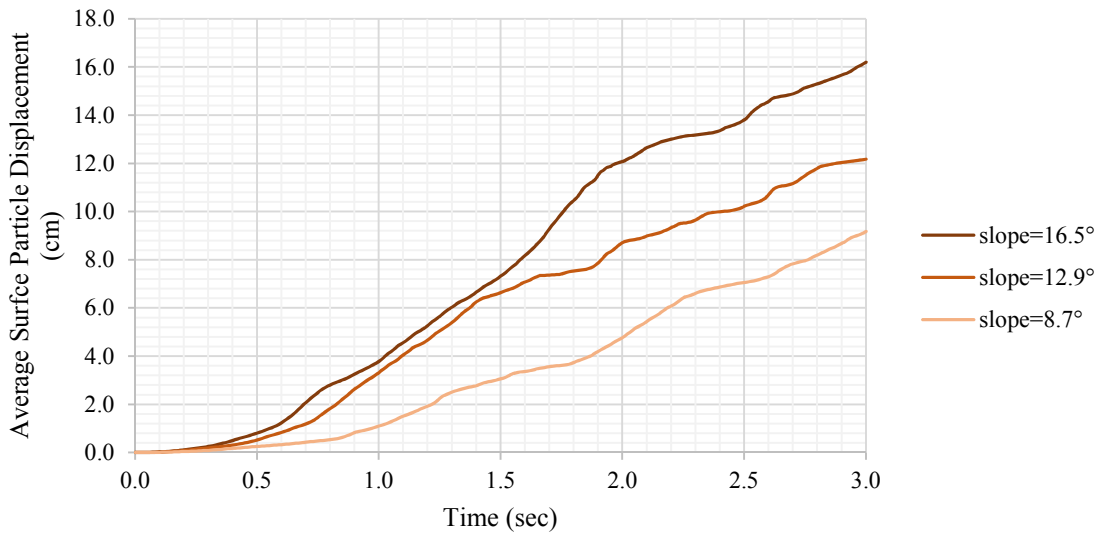


Figure 5-15 Average flow-generated displacement of surface particles of unreinforced packings with the same particle size distribution

The particle packings with steeper slopes generally experienced more flow-generated displacements. This is understandable since generally, surface particles of lower slopes are more stabilized by neighboring particles and therefore are able to resist higher runoff forces before getting displaced. Figure 5-13 also shows exceptions to this trend, where a packing with a lower slope, such as the 7.6° packing, has experienced more flow-generated displacements than a steeper

slope, such as the  $9.5^\circ$  slope. This could be due to the specifics of the surface particle configuration on the packing and surface irregularities that are not easy to measure, but can contribute considerably to either stabilizing or un-stabilizing the surface particles. Such local effects, which are anticipated in granular media, can result in higher or lower than expected flow-generated displacements for a period of time during the simulation. It may also be related to the random nature of the initial packings. This shows the importance of investigating various particle packings in order to attain a governing trend in behavior.

Several simulations with various reinforcing schemes were carried out on different packings, to study the effect of slope reinforcements on flow-generated displacements. “Net” reinforcing pattern, shallow reinforcing of 25% of surface particles, deep reinforcing of 25% of surface particles and shallow reinforcing of 50% of surface particles were modeled and investigated. In order to be able to compare the results of the simulations, the same model properties listed in Table 4-1 were used in all simulations.

The net reinforcing pattern connects neighboring surface particles of a packing with reinforcing springs. Figure 5-15 shows the reinforced packings at  $t=0$  sec. The reinforcing springs are shown with a line connecting the particles. The 25% and the 50% shallow reinforcing patterns, respectively connect 25% and 50% of the surface particles to the particles beneath. These reinforcements are shallow and do not extend deep into the packing. Whereas the 25% deep reinforcing pattern connects the same surface particles to deeper particles in the packing. The reinforcing is manually assigned and distributed evenly throughout the surface. Figures 5-16 to 5-18 show the 25% shallow, 25% deep and 50% shallow reinforced particle packings.

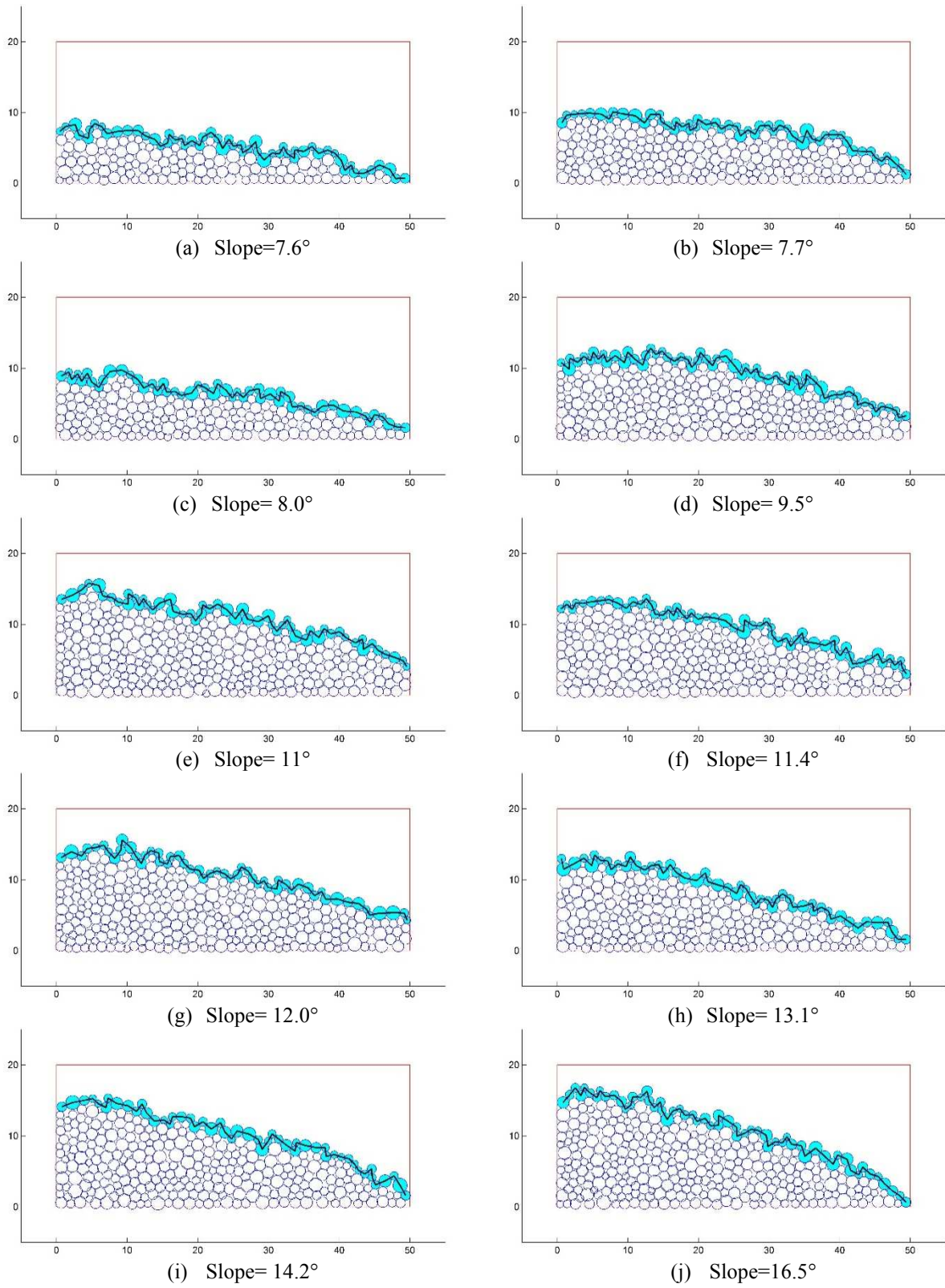


Figure 5-16 Particle packings reinforced with the net pattern

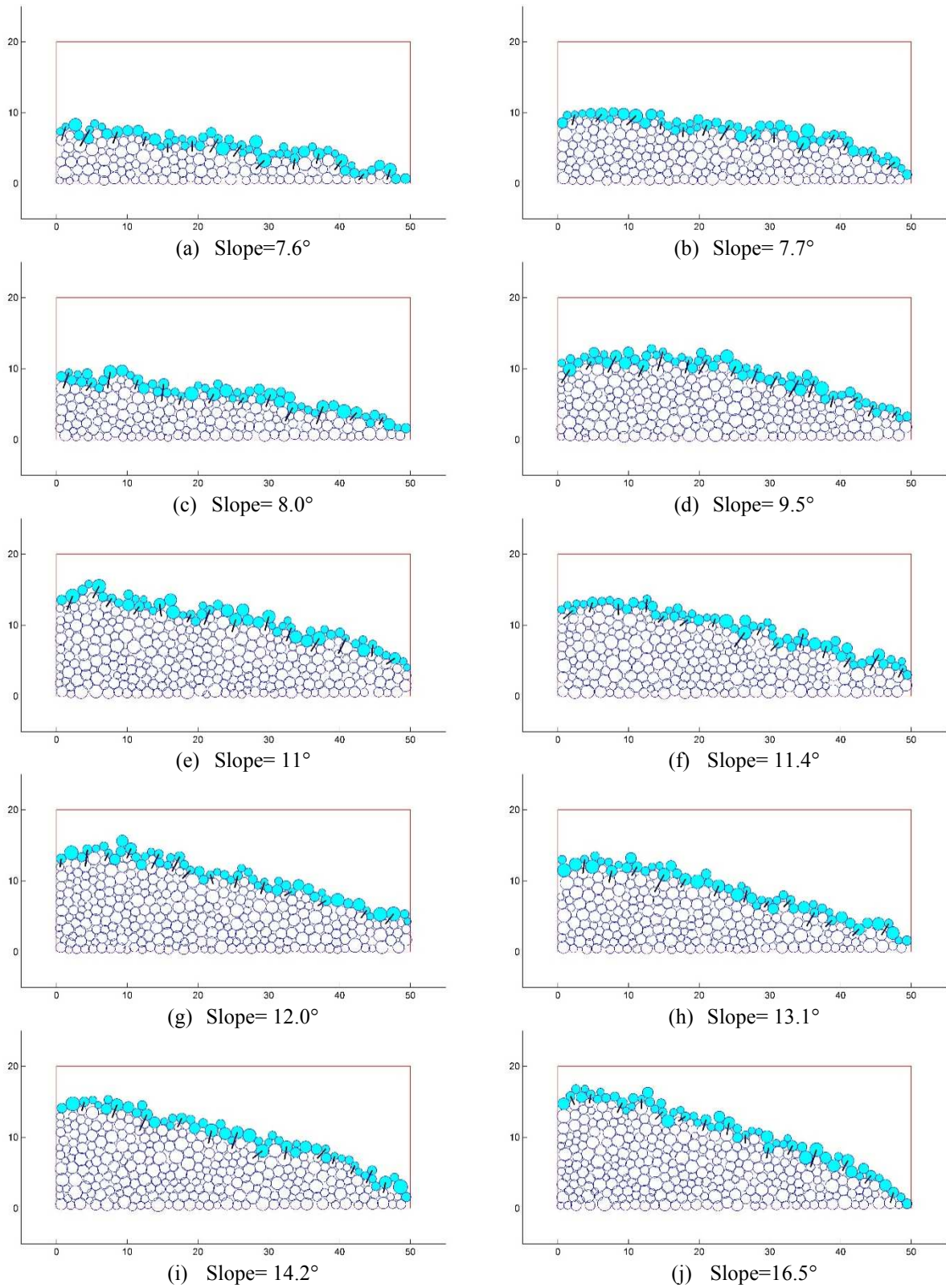


Figure 5-17 Particle packings reinforced with the 25% shallow reinforcing pattern

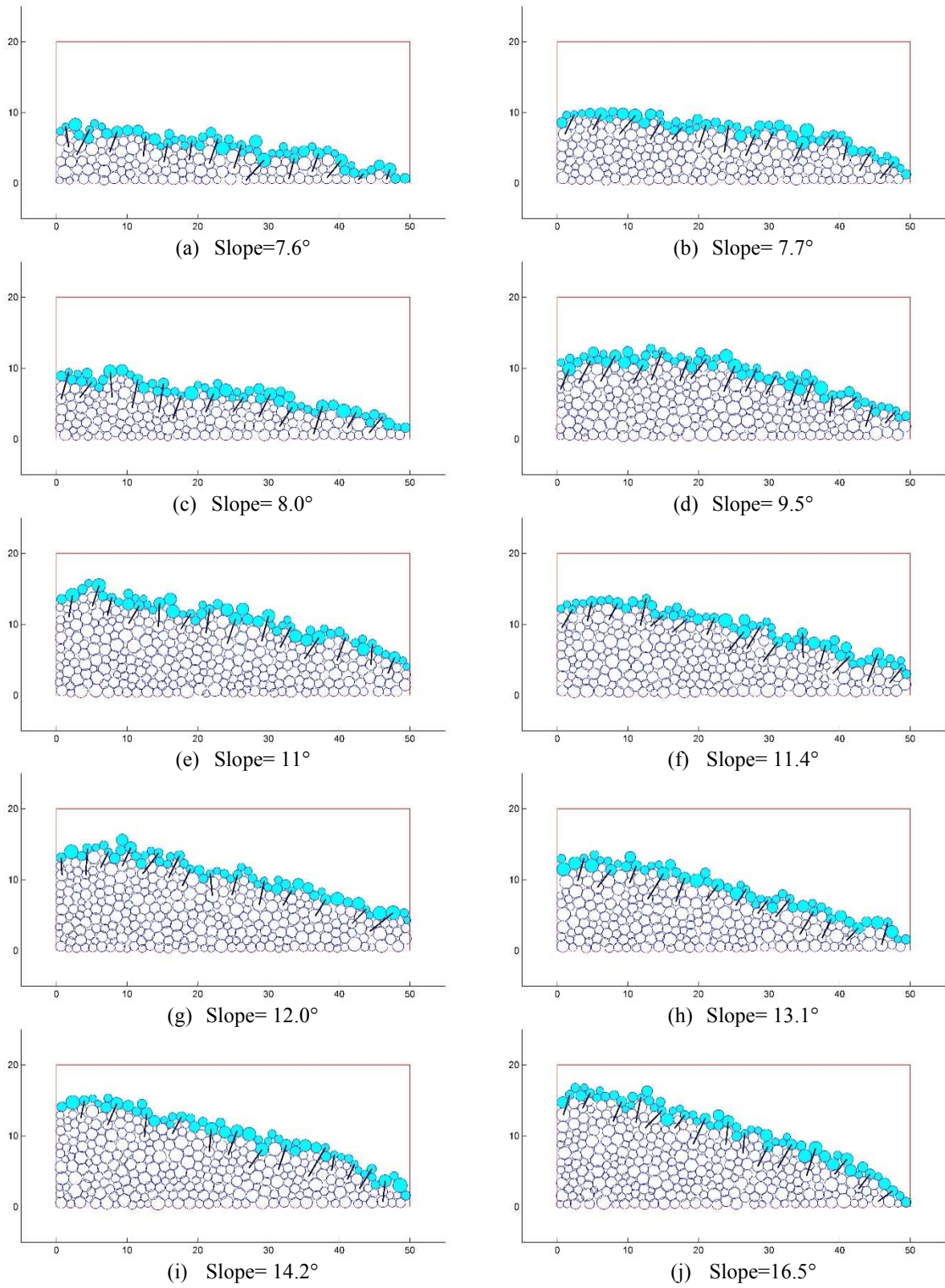


Figure 5-18 Particle packings reinforced with the 25% deep reinforcing pattern

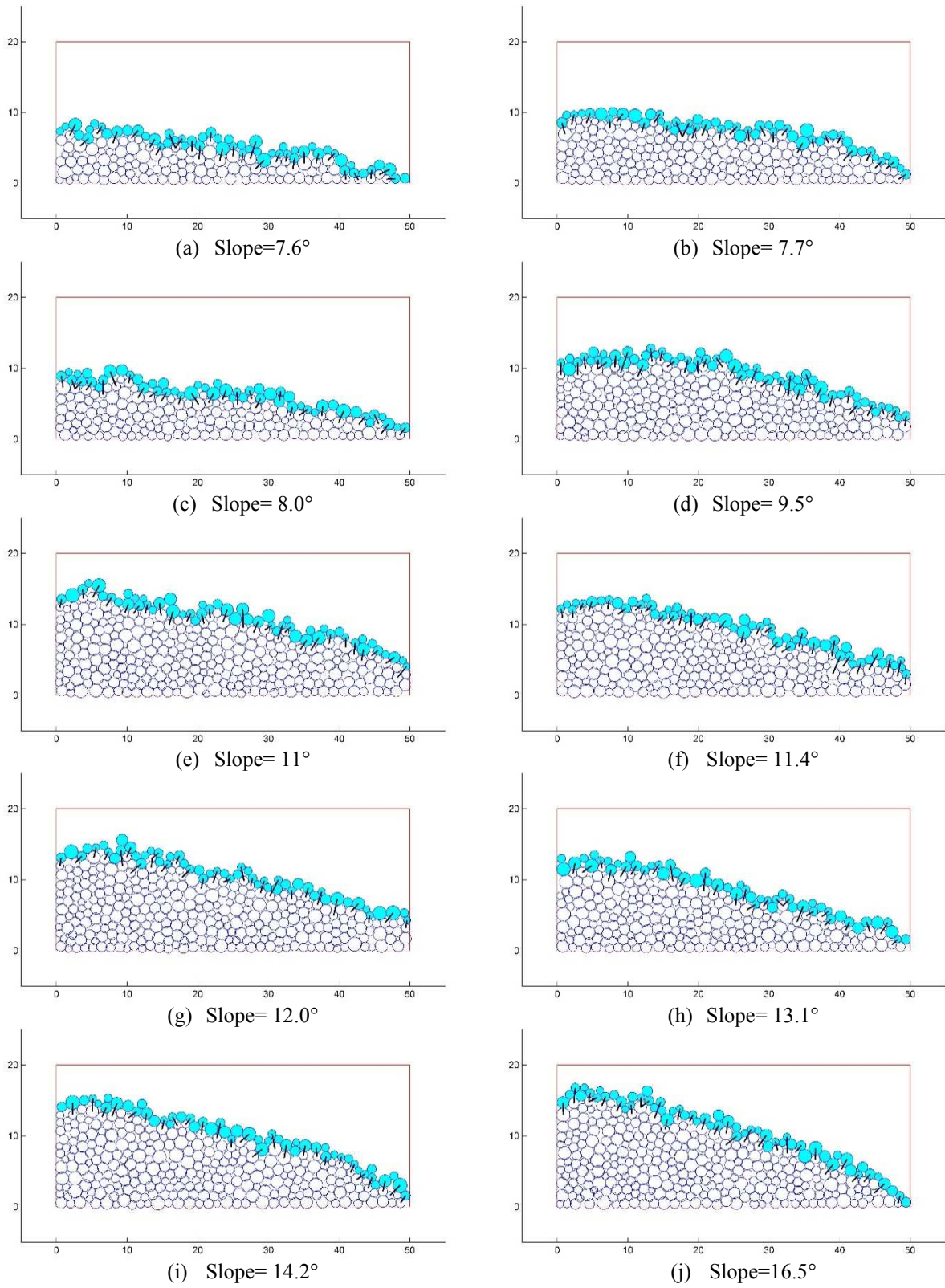


Figure 5-19 Particle packings reinforced with the 50% deep reinforcing pattern

Figure 5-20 shows the time-averaged average particle displacement of surface particles for the different packings with different reinforcing patterns. The packings with steeper slopes experienced more flow-generated displacements in general.

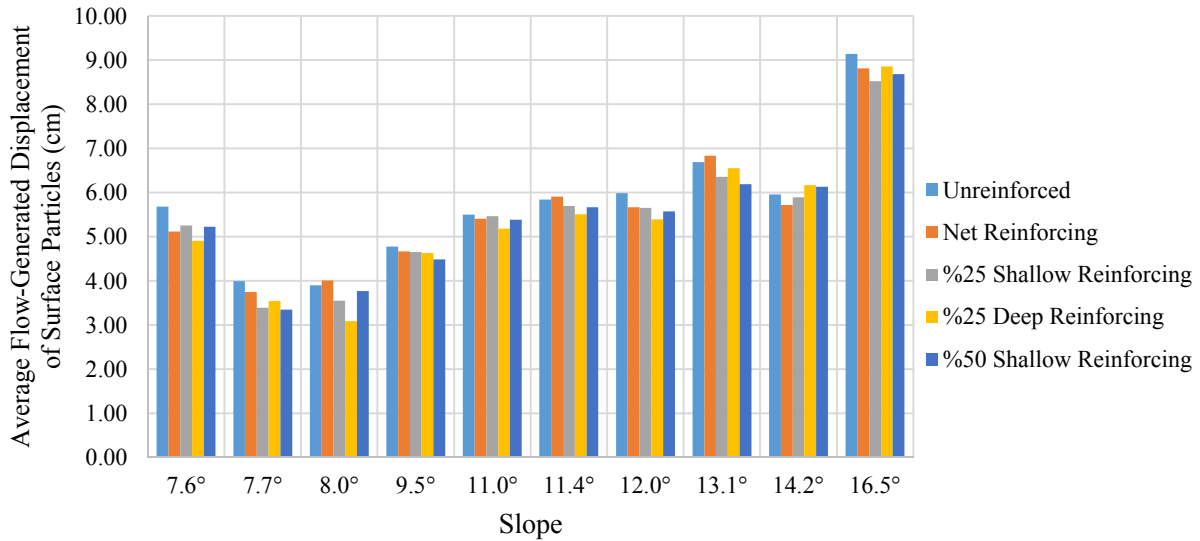


Figure 5-20 Time-averaged flow-generated displacements of the surface particles for packings

Figure 5-21 shows the percent change in flow-generated displacements of granular packings, comparing the different reinforcing schemes with the unreinforced condition. The effectiveness of the reinforcing patterns in reducing the flow-generated displacements varied for the different packings.

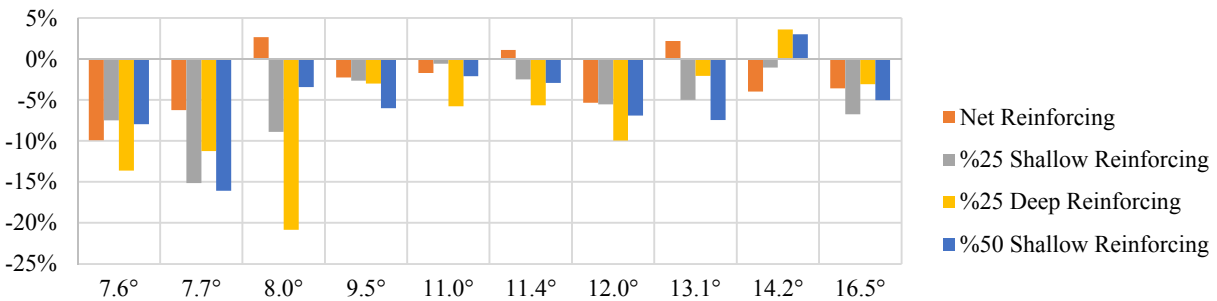


Figure 5-21 Percent Change in Average Flow-Generated Displacement of Surface Particles

### 5.2.2 Packings with Identical Particles

To eliminate the effect of the particle size distribution in the behavior of the particulate systems, three packings with identical particles and initial slopes of 8.7°, 12.9°, and 16.5° were

also studied. The reinforcing patterns used in the previous simulations were applied. Figures 5-22 shows the 8.7° and 12.9° packings with the different reinforcing patterns. The reinforcing patterns for the 16.5° slope were shown in the Figures 5-16(j) to 5-19(j).

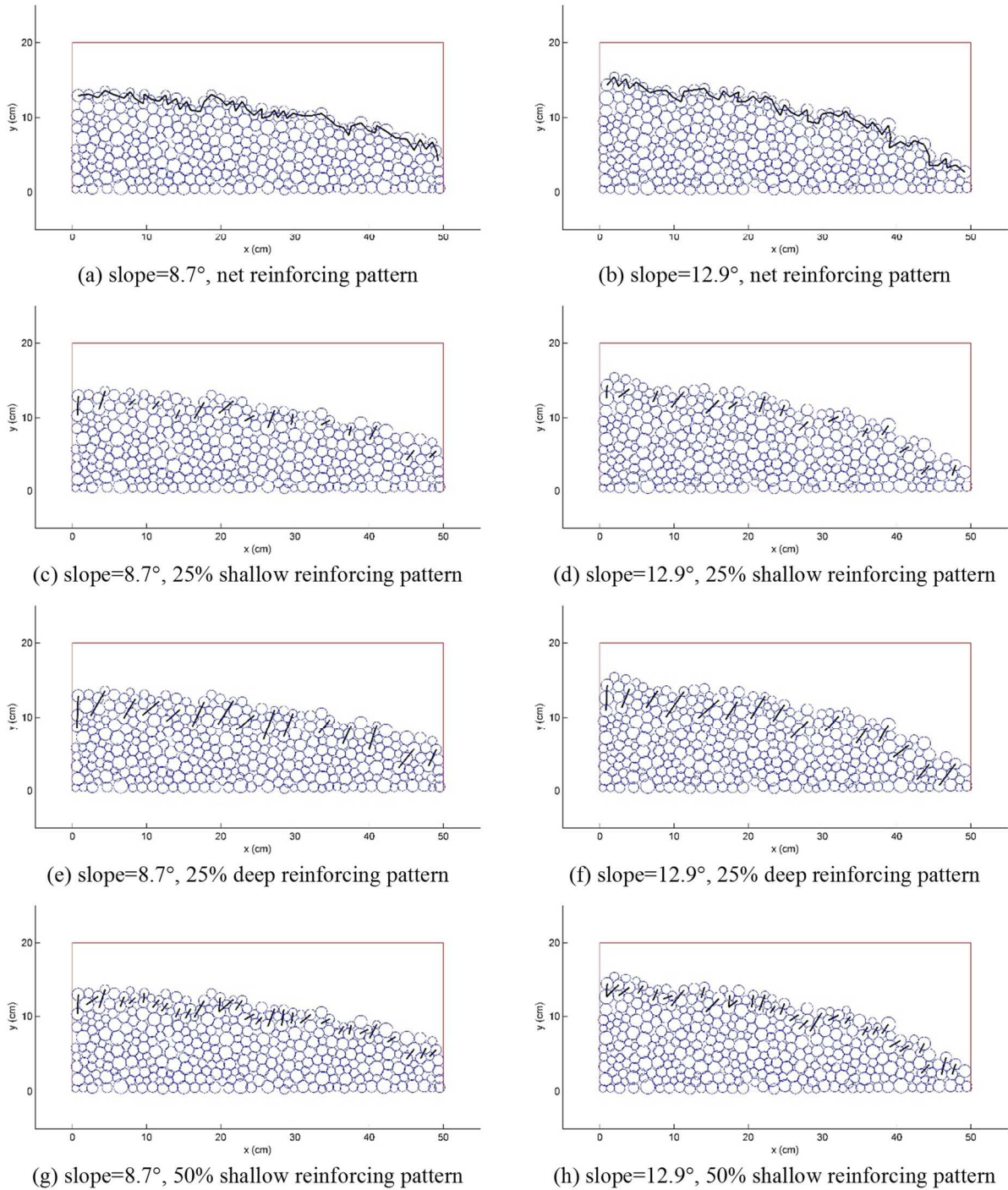


Figure 5-22 Reinforced packings with the same particle size distribution

In the first set of simulations, the surface particles exposed to the flow-generated drag forces were updated at each time-step to account for the changes in the surface after the initiation of flow. In each time-step, the two particles with the largest  $y$  within  $x < 4 \text{ cm}$  and  $x > 48 \text{ cm}$  were found and the particles above the line connecting those two particles were selected as surface particles and exposed to flow-generated forces. This resulted in variation of the number of surface particles during the simulation. This change was accounted for in the calculation of the average surface particle displacement at every time-step. In reality the particles exposed to the flow-generated forces change as the flow develops and the initial surface particles start to roll over the surface, however it was found that selecting the surface particles based on a line connecting a high and low particle on the sides of the packing was inadequate, and in many cases resulted in either a very thin or thick layer of surface particles.  $H = 4.0 \text{ N/m}$  was used in the simulations. In addition, simulations with 10% higher drag forces were carried out. Figure 5-23 shows the time-averaged average particle displacement of surface particles for the packings with the same particle size distribution for the different reinforcing patterns.

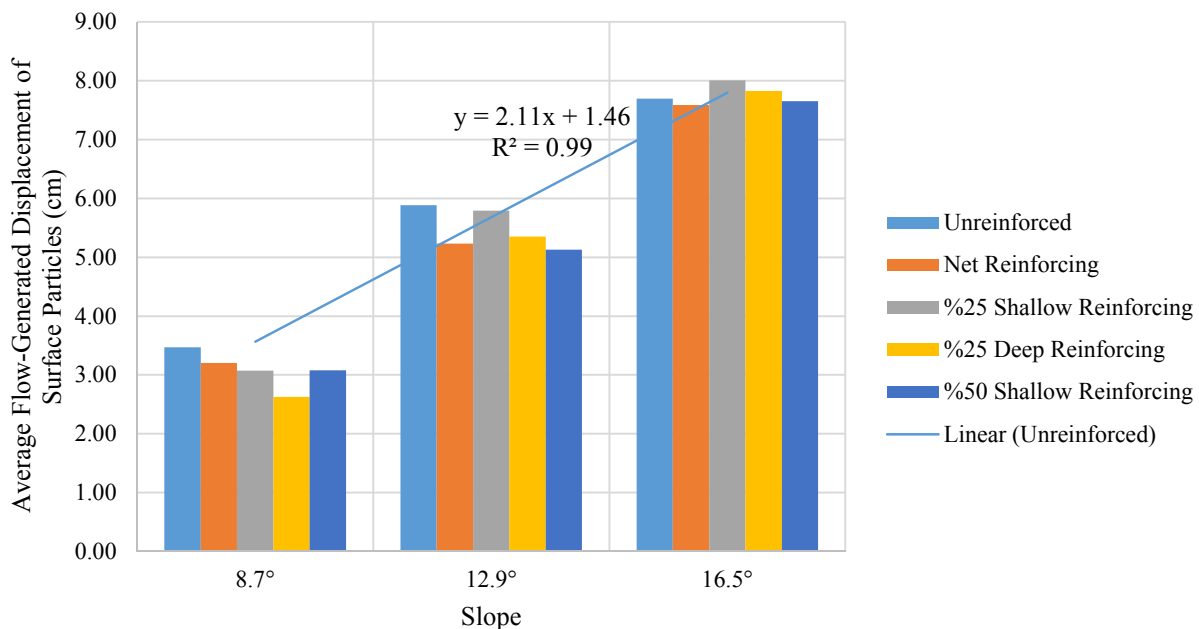


Figure 5-23 Time-averaged flow-generated displacements of surface particles of unreinforced and reinforced packings with the same particle size distribution

Figure 5-24 shows the percent change in average flow-generated displacements of granular packings with the same particle size distribution, comparing the different reinforcing schemes with the unreinforced condition. The difference between the results shown here for the 16.5° packing, and the results shown in Figure5-21 and Figure5-24. This is due to the different approaches for selecting the surface particles.

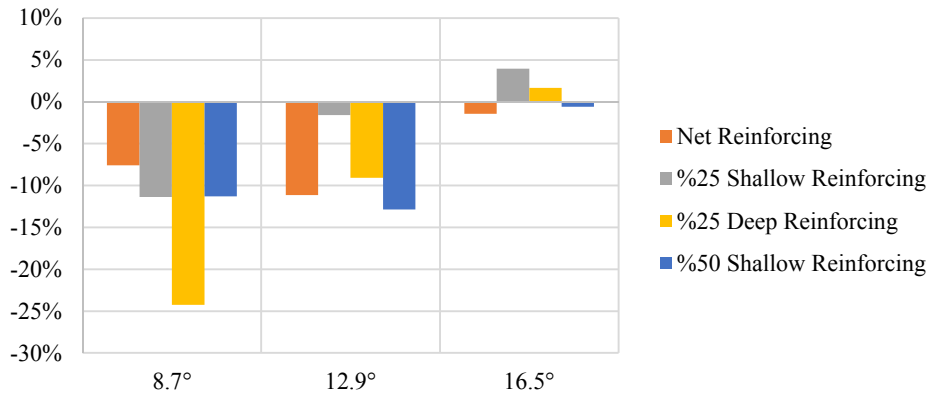


Figure 5-24 Percent change in average flow-generated displacement of surface particles for packings with the same particle size distribution

For the 8.7° and 12.9° packings, reinforcement reduced the flow-generated displacements of surface particles from 2% to 24%. However, for the 16.5° packing, all reinforcing patterns, except for the net pattern, increased the flow-generated displacements, compared to the non-reinforced slope. The effectiveness of the different reinforcing patterns in reducing the flow-generated displacements varies from one packing to another.

Figure 5-25 shows the percent change in average flow-generated displacements of granular packings with the same particle size distribution due to a 10% increase in applied drag flow-generated forces. The increase in the applied drag force has resulted in 3% to 45% increase in the flow-generated displacements, with the maximum effect on the lower slope of 8.7°. The unreinforced 12.9° packing has experienced a 7% decrease in displacements. Figure 5-26 shows the average surface particle displacements during the simulation of the unreinforced 12.9° slope

for the basic ( $H = 4.0$ ) and increased drag forces ( $H = 4.4$ ). It can be seen that rate of increase in the flow-generated displacements for the  $H = 4.4$  simulation suddenly decreases at about  $t = 2 \text{ sec}$  which has resulted in the decrease of the overall average flow-generated displacements, compared to the  $H = 4.0$  simulation. This is probably due the fact that the particle layout has resulted in a very thin layer of detected surface particles the linear surface definition.

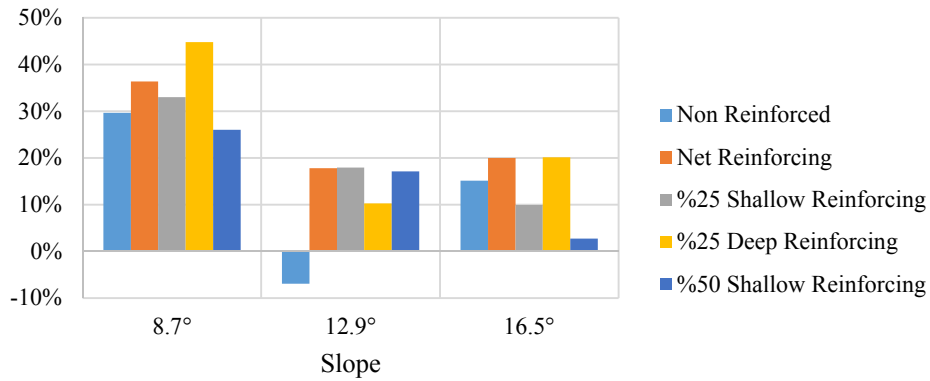


Figure 5-25 Percent change in average flow-generated displacement of surface particles for packings with the same particle size distribution due to %10 increase in drag force

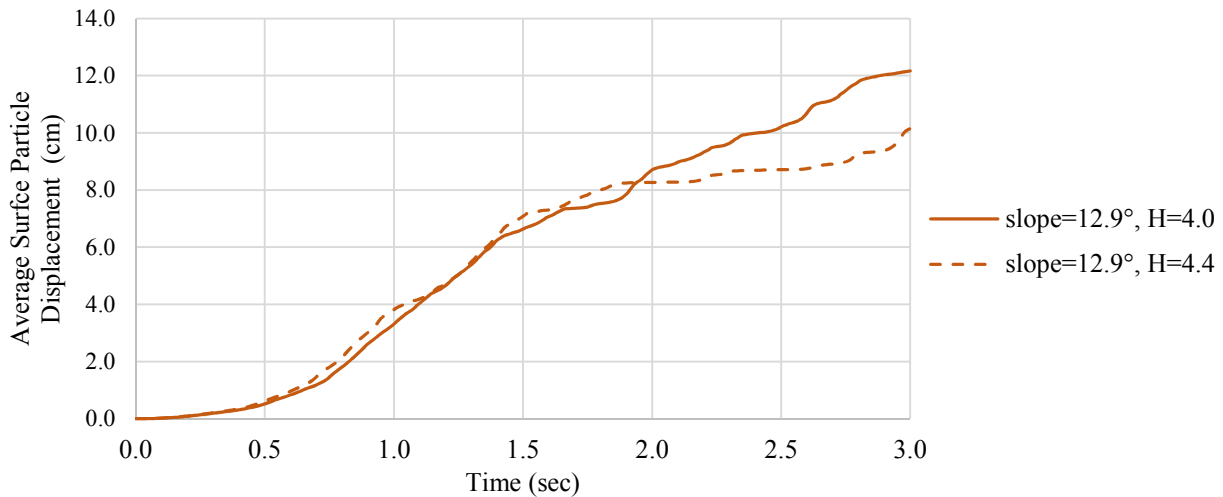


Figure 5-26 Average flow-generated displacement of surface particles of unreinforced 12.9° slope

Due to inadequacy of the linear surface detection algorithm, a more advanced algorithm was developed and another set of simulations were carried out on the three packings with identical particles. The more advanced algorithm detected and updated the surface particles every  $0.01 \text{ sec}$ .

This method was found to be considerably more accurate in selecting surface particles throughout the simulations and therefore improved the application of the flow-generated forces and eliminated the errors resulting from sudden changes in the number of surface particles. Also, the stiffness and strength of the reinforcement were increased to see how ultimately effective they are. A reinforcing spring stiffness of  $K_r = 100 K_n$  was used and the breaking criteria for the reinforcement was removed so that they would remain active throughout the simulation. Figure 5-27 shows the average flow generated displacement of all particles for the unreinforced and reinforced slopes for  $H = 3.2 \text{ N/m}$ .

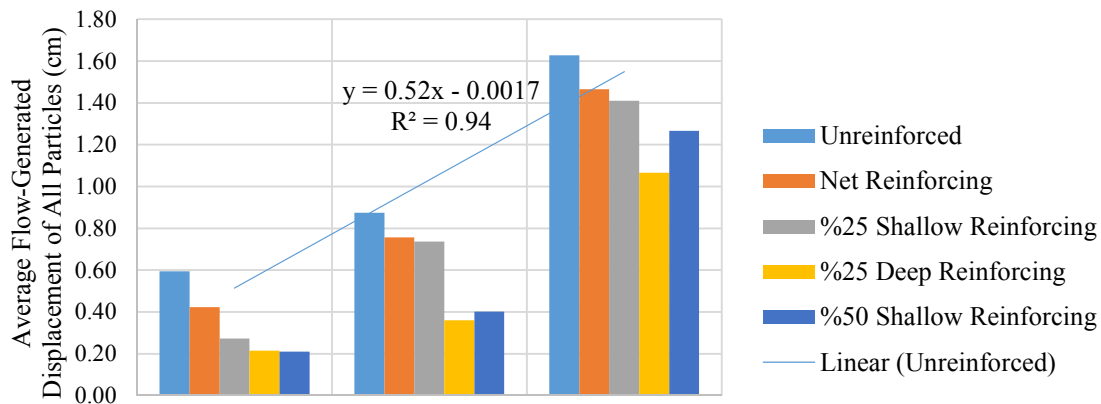


Figure 5-27 Time-averaged flow-generated displacements of unreinforced and reinforced packings with the same particle size distribution for  $H=3.2 \text{ N/m}$

Packings with higher initial slopes experienced more flow-generated displacements and the reinforcement was found to reduce the displacements in all cases. Figure 5-28 shows the percent change in average flow-generated displacements due to reinforcing. The different reinforcing patterns reduced the displacements from 10% to 65%, and were found to be most effective in the packing with the lowest slope ( $8.7^\circ$ ), causing 29% to 65% decrease in the flow-generated displacements. The 25% deep and the 50% shallow reinforcing patterns were found to be the most effective pattern for the three packings.

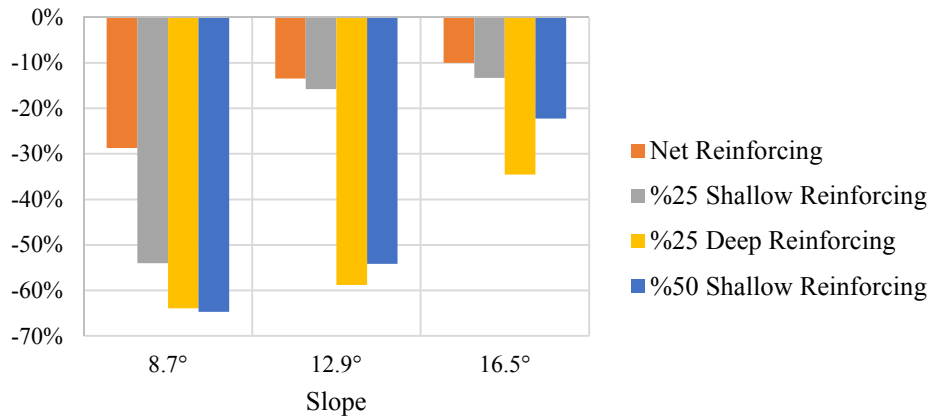


Figure 5-28 Percent change in flow-generated displacements of packings with the same particle size distribution for  $H=3.2$  N/m

Figure 5-29 shows the maximum force developed in the reinforcing springs during the simulations that ranged from 0.24 to 0.67 Newtons.

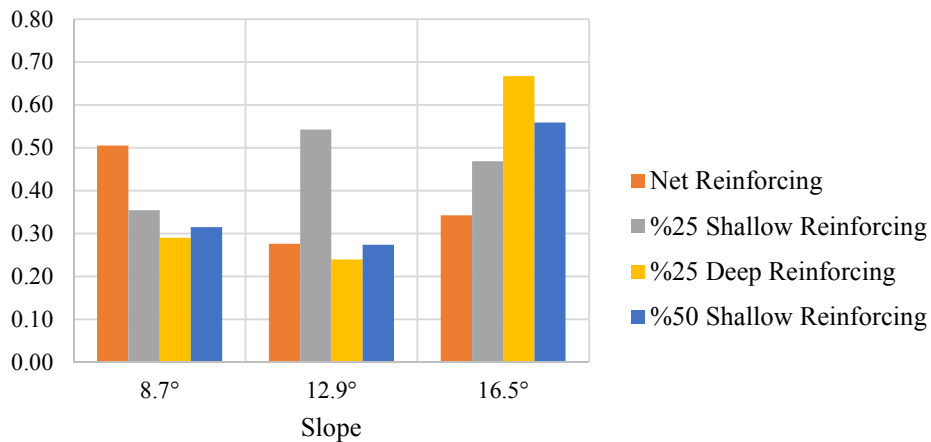


Figure 5-29 Maximum tension force in reinforcing springs for packings for  $H=4.0$  N/m

The same simulations were carried out with a 25% increase in drag force. Figure 5-30 shows the average flow generated displacement of all particles for the unreinforced and reinforced slopes for  $H = 4.0$  N/m. Again, packings with higher initial slopes experienced more flow-generated displacements and the reinforcement was found to reduce the displacements in all cases.

Figure 5-31 shows the percent change in average flow-generated displacements due to reinforcing. The different reinforcing patterns reduced the displacements from 11% to 64%, and where found to be most effective in the packing with the lowest slope (8.7°). Comparison of Figure

5-28 for  $H = 3.2 \text{ N/m}$  and Figure 5-30 for  $H = 4.0 \text{ N/m}$ , shows that the effectiveness of each reinforcing pattern in reducing the displacements of each packing did not change significantly with the increase in the drag force.

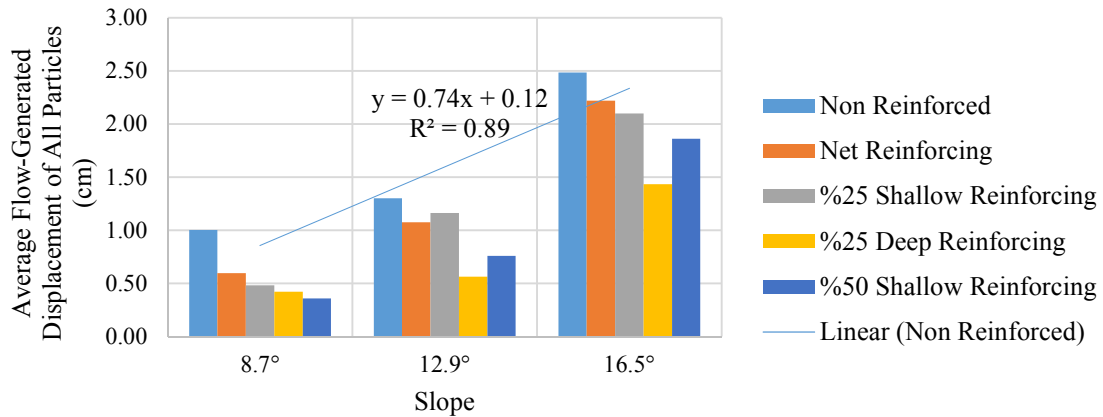


Figure 5-30 Time-averaged flow-generated displacements of unreinforced and reinforced packings with the same particle size distribution for  $H=4.0 \text{ N/m}$

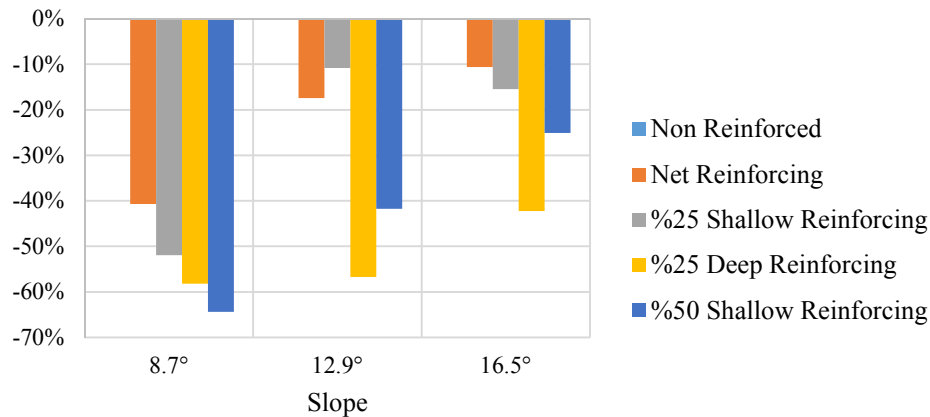


Figure 5-31 Percent change in flow-generated displacements of packings with the same particle size distribution for  $H=4.0 \text{ N/m}$

Figure 5-32 shows the percent change in flow-generated displacements of unreinforced and reinforced packings, due to 25% increase in the drag force. The displacements increased from 35% to 96%. This shows the significance of the effect of the amount of drag force applied on flow-generated displacements.

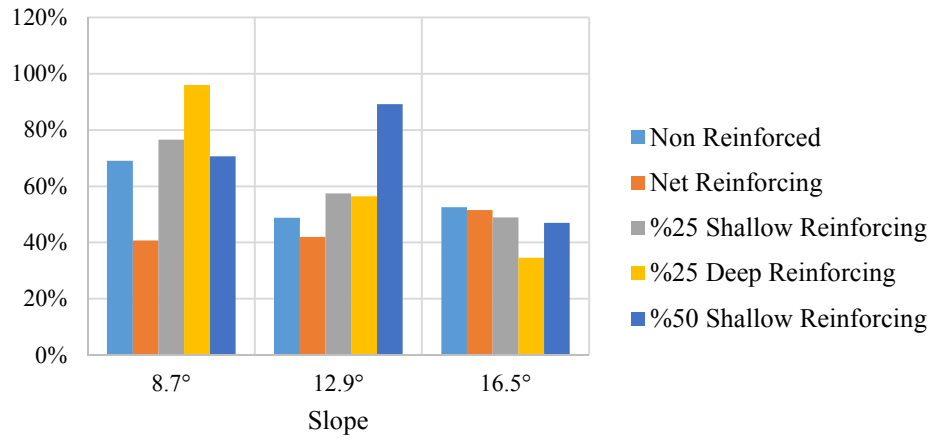


Figure 5-32 Percent change in flow-generated displacements of unreinforced and reinforced packings with the same particle size distribution due to 25% increase in the drag force

## 6. SUMMARY AND CONCLUSIONS

This study investigated the flow-generated displacements of 13 planar granular packings with slopes ranging from  $7.6^\circ$  to  $16.5^\circ$  and with particle radii from 5 to 10 *mm*. The granular packings were simulated using the DEM. A no-tension linear spring-dashpot model was used for the normal contact and a linear spring-dashpot model combined with Coulomb friction law was used for the tangential contact. Collision of a particle with a rigid wall and collision of two particles were simulated and compared with analytical solutions for validation of the model. Unreinforced and reinforced packings, where the reinforcement was applied using several differing methodologies, were exposed to flow-generated forces that simulated the effects of flowing water. The displacements of the surface particles and the effect of the reinforcing patterns were investigated to determine the relative level of influence of these reinforcement schemes. The following summarizes the main conclusions.

From comparison of analytical solutions with simulation results it was concluded that:

- The effect of global damping was found to be less significant when contact damping was increased.
- When global damping was not applied to particle collisions, kinetic energy of the system dissipated up to 50% as the contact damping coefficient,  $\beta$ , was increased to 0.1.
- The error in calculation of particle velocities after collision, decreased from 6% to 0.01% as the contact damping coefficient was increased from zero to 0.1. The error was the smallest when the contact force was modeled as an over-damped spring-dashpot model, and the difference between the simulation results and the analytical solution was found to be negligible, less than 0.16%, throughout the collision.

From the study of flow-generated displacements of the packings with varying slopes and reinforcement, it was concluded that:

- In 35 out of the 40 simulations carried out on 10 packings with various particle size distributions, surface reinforcement reduced the flow-generated displacements of surface particles. The reinforcement was found to be more effective in lower slopes.
- The effectiveness of the different reinforcing patterns in reducing the flow-generated displacements varied significantly for packings with various particle size distributions.
- Use of packings with the same particle size distribution and correct selection of surface particles exposed to the flow-generated forces was crucial to realistically model of the behavior and obtain reliable results.
- The particle packings with steeper slopes generally experienced more flow-generated displacements. For packings with the same particle size distribution, the average displacement of particles was found to increase linearly with slope and could be predicted using  $\overline{\Delta S} = 0.52 \times \text{slope}$  and  $\overline{\Delta S} = 0.74 \times \text{slope} + 0.12$  for flow velocity of 0.65 and 0.73 *m/sec* respectively. ( $\overline{\Delta S}$  in *cm* and slope in degrees)
- In the simulations carried out on packings with the identical group of particles and varying slopes, reinforcement reduced the displacements in all simulations, anywhere from 10% to 65%. The reinforcing was found to be most effective in the packing with the lowest slope (8.7°), causing 29% to 65% decrease in the flow-generated displacements.
- For packings with the identical group of particles, the 25% deep and the 50% shallow reinforcing patterns were the most effective patterns and reduced the flow-generated displacements by 32% to 65%.

- The effectiveness of the different reinforcing patterns in reducing the displacements was independent of the amount of drag force applied, for the two force magnitudes tested.
- A 25% increase in the applied flow-generated forces resulted in 35% to 96% increase in the flow-generated displacements of particle packings with identical particles and varying reinforcing patterns.

Considering the results and the limitations of the scope of this study, the following steps are recommended for future research:

- In this study the validation of the DE model was limited to comparison of results with analytical results of simple cases of particle-wall and particle-particle collisions. The reliability of results could be improved if the parameters of the model are selected based on the comparison of results of the DE model with experimental tests.
- In this study the simulations were limited to planar assemblies and the interactions of particles in the third dimension were not taken into account. It is recommended that the simulations be extended to three-dimensional assemblies.
- Circular particles were used in this study whereas the real shapes of soil particles are very irregular. Such irregularities cause interlocking of particles and produce tangential forces that could affect flow-generated displacements. It is recommended that either more complex shapes be modeled in future studies or that the tangential contact force model is improved to better incorporate the interlocking effects.
- Due to computational limitations, the assembly used in this study was limited to 350 particles with radii between 5 and 10 *mm*. It is recommended that future studies extend to larger assemblies with smaller sized particles, to better represent the behavior of real soil particles.

## REFERENCES

- Abbaspour-Fard, Mohammad Hossein. 2000. *Discrete element modelling of the dynamic behaviour of non-spherical particulate materials*. University of Newcastle upon Tyne: Department of Agricultural and Environmental Sciences.
- Campbell, C. S., and C. E. Brennen. 1983. "Computer simulation of shear flows of granular material." In *Mechanics of granular materials: New models and constitutive relations*, 313-326. Amsterdam: Elsevier Science Publishers B.V.
- Cazzuffi, Daniele, Giuseppe Cardile, and Domenico Gioffrè. 2014. "Geosynthetic Engineering and Vegetation Growth in Soil Reinforcement Applications." *Transportation Infrastructure Geotechnology* 262-300.
- Cleary, Paul W., and David Hoyer. 2000. "Centrifugal mill charge motion and power draw: comparison of DEM predictions with experiment." *International Journal of Mineral Processing* 59 131-148.
- Cui, Liang, and Catherine O'Sullivan. 2003. "Analysis of a triangulation based approach for specimen generation for discrete element simulations." *Granular Matter* 5 135-145.
- Cundall, P. A. 1988. "Formulation of a three-dimensional distinct element model - part I. A scheme to detect and represent contacts in a system composed of many polyhedral blocks." *International Journal Of Rock Mechanics And Mining Sciences & Geomechanics Abstracts*, 25(3) 107-116.
- Cundall, P. A., and O. D. L. Strack. 1979. "A discrete numerical model for granular assemblies." *Géotechnique* 29(1) 47-65.
- Di Renzo, Alberto, and Paolo Di Maio. 2004. "Comparison of contact-force models for the simulation of collisions in DEM-based granular flow codes." *Chemical Engineering Science* 59 525-541.
- Feng, Y. T., K. Han, and D. R. J. Owen. 2003. "Filling domains with disks: an advancing front approach." *International Journal for Numerical Methods in Engineering* 56 699-713.
- Ferrellec, Jean-Francois, and Glenn R. McDowell. 2010. "A method to model realistic particle shape and inertia in DEM." *Granular Matter* 459-467.
- Grasselli, Y., and H. J. Herrmann. 1997. "On the angles of dry granular heaps." *Physica A* 246 301-312.
- Grima, Andrew Phillip, and Peter Wilhelm Wypych. 2011. "Development and validation of calibration methods for discrete element modelling." *Granular Matter* 127-132.
- Hoerner, Sighard F. 1965. *Fluid-dynamic drag; practical information on aerodynamic drag and hydrodynamic resistance*. Midland Park: N.J.

- Huang, Xin, Kevin J. Hanley, Catherine O'Sullivan, and Fiona C.Y. Kwok. 2014. "Effect of sample size on the response of DEM samples with arealistic grading." *Particuology* 107–115.
- Hungr, Oldrich. 2008. "Simplified models of spreading flow of dry granular material." *Canadian Geotechnical Journal* 1156-1168.
- Jensen, Richard P., Peter J. Bosscher, Michael E. Plesha, and Tuncer B. Edil. 1999. "DEM Simulation of granular media-structure interface: Effects of surface roughness and particle shape." *International Journal for Numerical and Analytical Methods in Geomechanics* 23 531-547.
- Jodrey, W. S., and E. M. Tory. 1985. "Computer simulation of close random packing of equal spheres." *Physical Review A, Volume 32, Number 4* 2347-2351.
- Krugger-Emden, H., E. Simsek, S. Rickelt, S. Wirtz, and V. Scherer. 2007. "Review and extension of normal force models for the Discrete Element Method." *Powder Technology* 171 157–173.
- Li, Yanjie, Yong Xu, and Colin Thornton. 2005. "A comparison of discrete element simulations and experiments for 'sandpiles' composed of spherical particles." *Powder Technology* 219-228.
- Lin, X., and T.-T. Ng. 1997. "A three-dimensional discrete element." *Géotechnique* 47(2) 319-329.
- Liu, S. H. 2006. "Simulating a direct Shear box test by DEM." *Canadian Geotechnical Journal* 155-168.
- Luding. 2008. "Introduction to discrete element methods : basic of contact force models and how to perform the micro-macro transition to continuum theory." *European Journal of Environmental and Civil Engineering*, 12 (7-8) 785-826.
- Luding, S. 1998. "Collisions & contacts between two particles." In *Physics of dry granular media*, 285-304. Springer Netherlands.
- Marketos, G., and C. O'Sullivan. 2013. "A micromechanics-based analytical method for wave propagation through a granular material." *Soil Dynamics and Earthquake Engineering* 45 25-34.
- Matuttis, H. G., S. Luding, and H. J. Herrmann. 2000. "Discrete element simulations of dense packings and heaps made of spherical and non-spherical particles." *Powder Technology* 109 278-292.
- Mirghasemi, A. A., L. Rothenburg, and E. L. Matyas. 1997. "Numerical simulations of assemblies of two-dimensional polygon-shaped particles and effects of confining pressure on shear strength." *Soils and Foundations*, Vol. 37, No. 3 43-52.
- Munjiza, A. 2004. "Munjiza-NBS contact detection algorithm in 2D." In *The combined finite-discrete element method*, 102-117. Hoboken, NJ: Wiley.

- Ng, Tang-Tat. 1994. "Numerical simulations of granular soil using elliptical particles." *Computers and Geotechnics* 16 153-169.
- O'Sullivan, Catherine. 2011. "Particle-based discrete element modeling: Geomechanics perspective." *International Journal of Geomechanics* 449-464.
- Poschel, Thorsten, and Thomas Schwager. 2005. *Computational granular dynamics*. Berlin: Springer-Verlag.
- Salciarini, Diana, Claudio Tamagnini, and Pietro Conversini. 2010. "Discrete element modeling of debris-avalanche impact on earthfill barriers." *Physics and Chemistry of the Earth* 35 172-181.
- Schafer, J., S. Dippel, and D. E. Wolf. 1996. "Force schemes in simulations of granular materials." *Journal de Physique I France* 6 5-20.
- Shmulevich, I. 2010. "State of the art modeling of soil-tillage interaction using discrete element method." *Soil and Tillage Research, Volume 111, Issue 1* 41-53.
- Sitharam, Thallak. G., S. V. Dinesh, and N. Shimizu. 2002. "Micromechanical modelling of monotonic drained and undrained shear behaviour of granular media using three-dimensional DEM." *International Journal for Numerical and Analytical Methods in Geomechanics* 26 1167-1189.
- Soga, K., E. Alonso, A. Yerro, K. Kumar, and S. Bandara. 2016. "Trends in large-deformation analysis of landslide mass movements with particular emphasis on the material point method." *Géotechnique* 66 248-273.
- Tijsskens, E., H. Ramon, and J. De Baerdemaeker. 2003. "Discrete element modelling for process simulation in agriculture." *Journal of Sound and Vibration* 266 493-514.
- Ting, John M., Brent T. Corkum, Claudia R. Kauffman, and Carlo Greco. 1989. "Discrete numerical model for soil mechanics." *Journal of Geotechnical Engineering* 115(3) 379-398.
- Zhou, Y. C., B. H. Xu, A. B. Yu, and P. Zulli. 2002. "An experimental and numerical study of the angle of repose of coarse spheres." *Powder Technology* 125 45-54.
- Zhu, H. P., Z. Y. Zhou, R. Y. Yang, and A. B. Yu. 2007. "Discrete particle simulation of particulate systems: Theoretical developments." *Chemical Engineering Science* 62 3378-3396.

# APPENDIX A

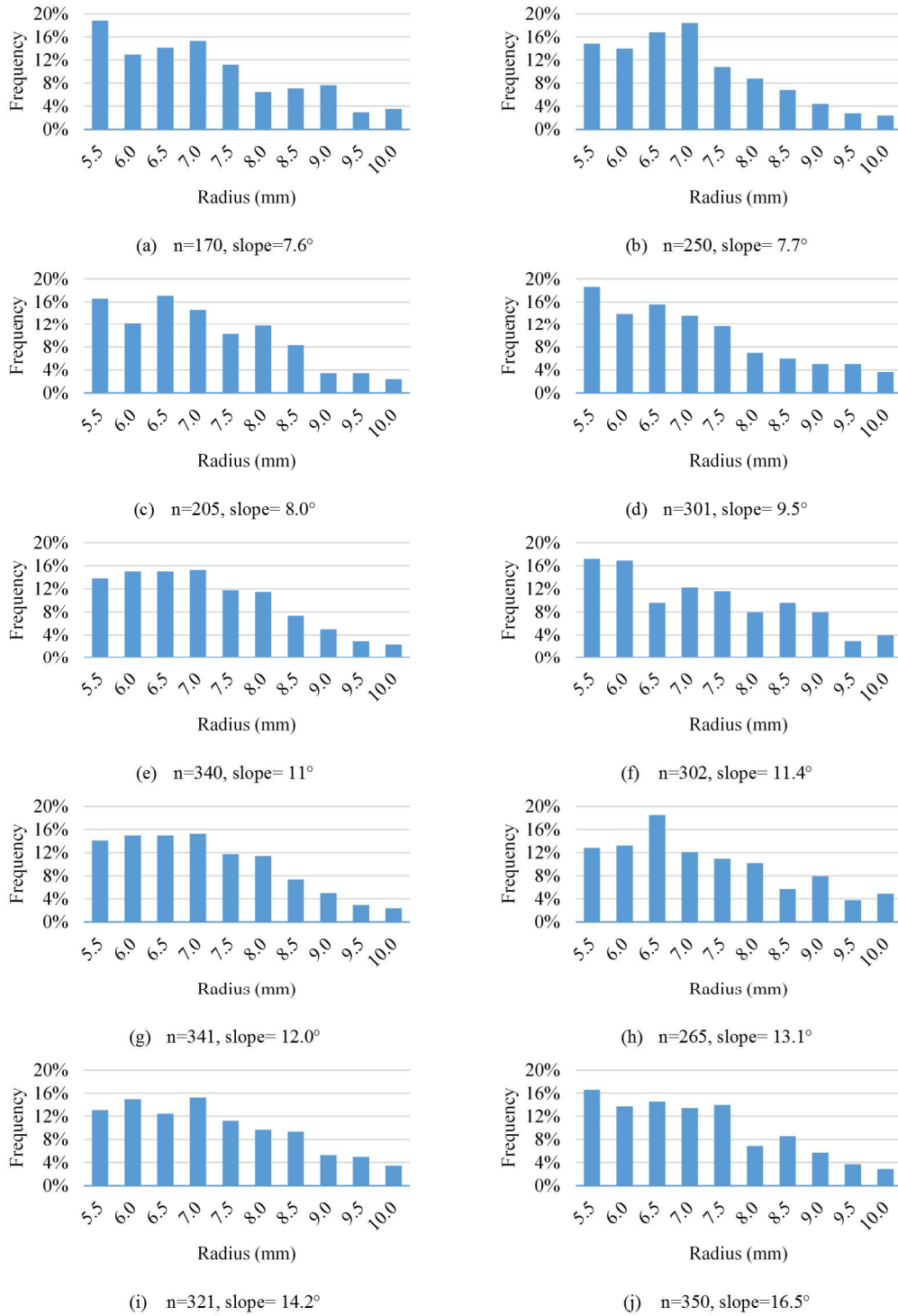


Figure A-1 Particle size distribution of packings shown in Figure 4-3